Computationally Efficient Nanophotonic Design through Data-Driven Eigenmode Expansion

by

Mehmet Can Oktay

A Dissertation Submitted to the
Graduate School of Sciences and Engineering
in Partial Fulfillment of the Requirements for
the Degree of

Master of Science

in

Electrical and Electronics Engineering

KOÇ ÜNİVERSİTESİ

August 6, 2024

Computationally Efficient Nanophotonic Design through Data-Driven Eigenmode Expansion

Koç University

Graduate School of Sciences and Engineering

This is to certify that I have examined this copy of a master's thesis by

Mehmet Can Oktay

and have found that it is complete and satisfactory in all respects,

and that any and all revisions required by the final

examining committee have been made.

Committee Members:

Assist. Prof. Emir Salih Mağden (Advisor)

Assoc. Prof. Muhammed Fatih Toy

Prof. Alper Kiraz

Date:

Dedicated to my parents and Miço

ABSTRACT

Computationally Efficient Nanophotonic Design through Data-Driven Eigenmode Expansion
Mehmet Can Oktay
Master of Science in Electrical and Electronics Engineering
August 6, 2024

Silicon photonic components require rapid design procedures with state-of-the-art optical metrics as the on-chip photonic applications advance. In this dissertation, a highly efficient and flexible method is introduced for designing a variety of low-loss waveguides in compact footprints. The proposed data-driven eigenmode expansion method represents waveguides as cascading eigenmode scattering matrices and propagation matrices. This method uses parallel data processing approaches to perform electromagnetic computations for simulating the optical response of individual waveguides in tens of milliseconds, orders of magnitude faster than the conventional methods, while achieving physical accuracies respected to 3D-FDTD. This framework, coupled with nonlinear optimization algorithms, designs adiabatic tapers, power splitters, and waveguide crossings that show near-lossless state-of-the-art operation within broad bandwidths. These devices and their 3D-FDTD simulations and experimental measurements highlight this methodology's capabilities and computational efficiency. A few photonic design problems currently under development will further demonstrate its applicability.

ÖZETÇE

Veri-Tabanlı Özkip Açılımı Yöntemi ile Yüksek Hesaplama Performanslı Nanofotonik Aygıt Tasarımı
Mehmet Can Oktay
Elektrik ve Elektronik Mühendisliği, Yüksek Lisans
6 Ağustos 2024

Silikon fotonik bileşenleri, çip üstü fotonik uygulamalar geliştikçe üstün optik metrikleri karşılayan hızlı tasarım prosedürleri gerektirir. Bu tezde, kompakt ayak izlerinde çeşitli düşük kayıplı dalga kılavuzları tasarlamak için oldukça verimli ve esnek bir yöntem tanıtılmaktadır. Önerilen veri odaklı özkip genişleme yöntemi, dalga kılavuzlarını basamaklı özkip saçılma matrisleri ve yayılma matrisleri olarak temsil eder. Bu yöntem, 3D-FDTD'ye göre fiziksel doğruluklar elde ederken, geleneksel yöntemlerden kat ve kat daha hızlı olan onlarca milisaniyede dalga kılavuzlarının optik tepkisini simüle etmek için elektromanyetik hesaplamalar gerçekleştirmek üzere paralel veri işleme yaklaşımlarını kullanır. Doğrusal olmayan optimizasyon algoritmalarıyla birleştirilen bu sistem, geniş bant genişliklerinde neredeyse kayıpsız son teknoloji işlemi gösteren adiabatik konikleştiriciler, güç bölücüler ve dalga kılavuzu geçişleri tasarlar. Bu cihazlar, 3D-FDTD simülasyonları ve deneysel ölçümleriyle birlikte, bu metodolojinin yeteneklerini ve hesaplama verimliliğini vurgulamaktadır. Şu anda geliştirilmekte olan birkaç fotonik tasarım problemi, uygulanabilirliğini daha da gösterecektir.

ACKNOWLEDGMENTS

I would like to extend my deepest appreciation and gratitude to the individuals who contributed to and supported me during my master's studies.

I want to express my most profound gratitude to Professor Emir Salih Mağden. He guided me throughout my research, starting from my undergraduate studies. We brought this research, which I dreamed of during the integrated photonics course, to maturity and proposed this method.

I want to thank Professor Emir Salih Mağden, Professor Muhammed Fatih Toy and Professor Alper Kiraz for taking the time to be on the jury committee of my thesis. The feedback I received from them played a significant role in completing my thesis.

Special thanks to the Scientific and Technological Research Council of Turkey (TUBITAK) for supporting my master's studies.

I'm also grateful to my colleagues in the Photonic Architecture Laboratories, especially Aytuğ Aydoğan, for their contributions.

I want to acknowledge the collaboration of Professor Lukas Chrostowski's Silicon Electronic Photonic Integrated Circuits (SiEPIC) program for their contribution to the fabrication and measurement of the devices to be mentioned.

I'm incredibly grateful to my family for being with me on this academic journey. They have always supported me, together with Miço.

TABLE OF CONTENTS

LIST OF TABLES

LIST OF FIGURES

ABBREVIATIONS

EM	Electromagnetic
ML	Machine Learning
FDTD	Finite Difference Time Domain
FDFD	Finite Difference Frequency Domain
EME	Eigenmode Expansion
SOI	Silicon On Insulator
GPU	Graphical Processing Unit
CPU	Central Processing Unit
ROMEO	Rapid Optical Eigenmode Optimizer
TE	Transverse Electric
EBL	Electronic Bill of Lading
SiEPIC	Silicon Electronic Photonic Integrated Circuits
PDK	Process Design Kit
SEM	Scanning Electron Microscope

Chapter 1

INTRODUCTION

1.1 Design Problem of Photonic Devices

The growing complexity of photonic applications and the developments in the integrated design space motivate the research for compact photonic building blocks satisfying sophisticated optical functionalities for next-generation photonic applications [Shekhar et al., 2024, Liu et al., 2022]. Imposing rigorous performance requirements for each building block's metrics, including near-lossless operation on wide transmission bandwidths [Asadinia et al., 2021, Chen et al., 2021, Riveros et al., 2021], is crucial for these systems to ensure steady optical performance in applications ranging from interferometry and communication to signal processing and on-chip sensing [Bogaerts et al., 2020, Feng et al., 2024]. Knowledge of fundamental waveguide theories and physical intuition can be valuable tools for designing high-performance optical waveguides; however, only using them might limit the device geometry's degrees of freedom, which can prohibit some application's design process [Goel et al., 2024].

1.2 Design Method: EM Simulations

ML-based approaches have recently become prominent in designing compact photonic components with the desired transmission performance [Yeung et al., 2023]. In these approaches, investigation for the most suitable optical metrics determines the design space, where the devices are represented with geometric parameters [Christiansen and Sigmund, 2021, Mao et al., 2023]. During this process, each iteration is often accompanied by FDTD [Tang et al., 2023] or FDFD [Wu et al., 2023] simulations to estimate the optical performance of each device geometry. Even though these EM simulations calculate the device response with sufficient physical accuracy, they demand computationally extensive operations as they solve EM equations on a finer spatial grid resolution. These operations, becoming consecutive in the optimization framework, become prohibitive with many iterations. On the other hand, the EME method, which is generally applied on larger devices, still needs to be adequately explored in photonic components' inverse design as a simulational tool. This method, traditionally 3D-accurate in a fully vectorial way, divides a given waveguide into consecutive cells and computes the respective scattering information of each simulated eigenmode in the propagation direction. When paired with modern data processing, EME can be remarkably efficient in iterative optimization schemes. It can be a pioneering method for designing high-performance photonic devices within compact footprints, satisfying the desired broadband optical functionalities for various on-chip optical applications.

1.3 Thesis Summary

This thesis introduces an innovative data-driven technique for photonic waveguide simulation and optimization by exploiting the synergy between ML and EME. Compared to the traditional EME, this method is based on an extensive database of waveguides with a wide range of widths simulated under several wavelengths, bypassing its intrinsic computational bottlenecks. This database, coupled with parallel computation improvements, allows the simulation of individual waveguides in several tens of milliseconds while keeping the physical accuracy matching the 3D-FDTD results in comparison to minutes or hours-long typical timeframes in other conventional EM simulations. This approach, combined with nonlinear optimization, rapidly calculates the waveguide's transmission characteristics and optimizes them with flexible parameters, simultaneously providing computational efficiencies and broad optical capabilities in photonic device design. This design paradigm is showcased through low-loss and high-performance adiabatic tapers, 1×2 power splitters, and waveguide crossings fabricated in the SOI platform. Also, its potential applicability for 2×2, 1×3 and 1×4 power splitters is further discussed. The proposed method exhibits new avenues for designing high-performance, broadband-integrated, and application-specific photonic devices with five orders of magnitude computational speed-ups compared to conventional approaches.

1.4 Thesis Organization

The thesis structure follows:

Chapter 2 dives deep into the EME and explains how the proposed method accelerates the conventional EME simulation. It introduces the necessary steps to design a waveguide.

Chapter 3 demonstrates that ROMEO can design waveguide tapers. It studies an optimized taper with 3D-FDTD simulations to demonstrate how well it allows the spatial evolution of the input mode [Oktay et al., 2022]. Also, it discusses the experimental results of the device in comparison with the literature.

Chapter 4 extends ROMEO's capabilities to design multiple output devices, such as 1×2 power splitters. It clarifies how ROMEO could design splitters with an additional matrix in its database. Furthermore, it verifies the optimized splitter with 3D-FDTD and examines its fabrication measurements, comparing it with the literature.

Chapter 5 discovers how ROMEO could design waveguide crossings. It explains how the 4-fold symmetry of these devices can enable the ROMEO framework to simulate such devices with the same database [Oktay et al., 2024a, Oktay et al., 2024b]. It documents the optimized crossing's 3D-FDTD and fabricated device spectrum and compares its bandwidth with the previously reported devices.

The Appendix elaborates on how the devices are fabricated, and measurements are conducted.

Chapter 2

DATA-DRIVEN EIGENMODE EXPANSION METHOD

2.1 *Conventional EME Pipeline*

The EME method constitutes the backbone of this dissertation. One must fully comprehend its pipeline to exploit this optical simulation's characteristics. Based on calculating the propagating eigenmodes' scattering at the boundaries between consecutive sections of a simulated waveguide structure and successively cascading them, EME simulates how any waveguide transfers the incoming eigenmodes. The device's overall performance, coupling between the incoming and outgoing modes, can be followed by the Overall Scatter Matrices, demonstrated in Equation 2.1, produced by the EME. It allows efficient simulation of devices of various lengths, thus being a valuable tool for the nanophotonic design of adiabatic structures with gradually changing widths. These simulations minimize the coupling to the undesirable eigenmodes of the device output plane by computing the transmission profile of pre-determined transverse structures.

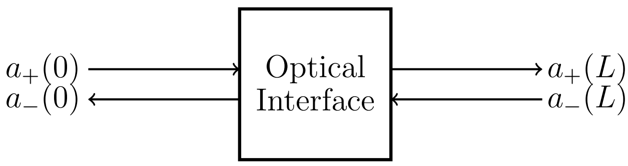

$$S_{mat} = \begin{bmatrix} S_{11} & S_{12} \\ S_{21} & S_{22} \end{bmatrix} \rightarrow \begin{bmatrix} a_-(0) \\ a_+(L) \end{bmatrix} = \begin{bmatrix} S_{11} & S_{12} \\ S_{21} & S_{22} \end{bmatrix} \begin{bmatrix} a_+(0) \\ a_-(L) \end{bmatrix} \tag{2.1}$$

Through consecutive device sections, EME cells, along the propagation direction, EME [Gallagher and Felici, 2003] solves Maxwell's equations in a bidirectional and vectorial manner. These computations are susceptible to the material and transverse geometry of the waveguide [Felici and Engl, 2001]; therefore, each brand-new waveguide demands a re-simulation of its transverse slices and their interfaces. Such computational bottlenecks preclude the EME's efficiency in optimization networks, where iteratively updating device geometry is followed by repetitive simulations.

For each consecutive simulation cell along the propagation direction, solutions to Maxwell's equations are stored as matrices in EME software. Firstly, the effective index (N_{eff}) is computed as an array; it shows how the eigenmodes are dispersed and how their phase characteristics, i. e. $B = i * \frac{2\pi}{\lambda} * N_{eff}$, will be during the propagation through the cell. As the height and material of the SOI platform is fixed throughout the device, N_{eff}'s are solely a function of the waveguide's width in that cell (W_{cell}). Besides, boundary conditions of the eigenmodes will change at the interfaces between consecutive cells as the W_{cell}s are changing, scattering the eigenmodes at these interfaces. By using overlap integrals on these incoming & outgoing eigenmodes, scatter matrices (S_{mat}) are computed. EME software calculates the overall performance based on N_{eff} arrays & S_{mat} matrices.

$$\begin{aligned}\mathbf{P_{mat}} &= \begin{bmatrix} 0 & P_{12} \\ P_{21} & 0 \end{bmatrix} \rightarrow \begin{bmatrix} a_-(0) \\ a_+(L) \end{bmatrix} = \begin{bmatrix} 0 & P_{12} \\ P_{21} & 0 \end{bmatrix} \begin{bmatrix} a_+(0) \\ a_-(L) \end{bmatrix} \\ &= \begin{bmatrix} 0 & & & & e^{B_1 * L} & & & \\ & 0 & & & & e^{B_2 * L} & & \\ & & \ddots & & & & \ddots & \\ & & & 0 & & & & e^{B_N * L} \\ e^{B_1 * L} & & & & 0 & & & \\ & e^{B_2 * L} & & & & 0 & & \\ & & \ddots & & & & \ddots & \\ & & & e^{B_N * L} & & & & 0 \end{bmatrix}\end{aligned} \tag{2.2}$$

To understand whether these are sufficient to realize any EME simulation, N_{eff} & S_{mat} for arbitrary device geometries are extracted. Then using the N_{eff} with L_{cell}, propagation matrices (P_{mat}) are computed, using the definition in Equation 2.2 for $N := N_{modes}$. After obtaining the respective P_{mat} and S_{mat} for each cell, the Overall Scatter Matrix is calculated by cascading them in sequential order (P_{mat}, S_{mat}, ...,

P_{mat}, S_{mat}, P_{mat}). Compared with the Lumerical simulation results [Lumerical, 2024], it becomes certain that device simulation can be performed by processing each cell's N_{eff} & S_{mat} information.

This implication revealed a compelling opportunity for the thesis, such that any waveguide can be characterized by a set of N_{eff} and S_{mat} pairs according to their sampling of cells. By constructing a database of these data, any device geometry can be represented and simulated without conventional EME.

2.2 *EME Database*

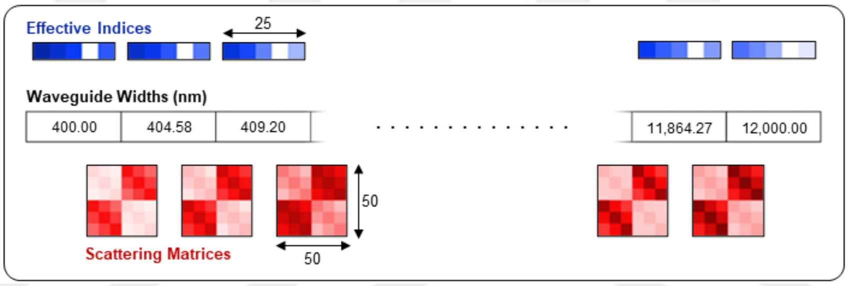

Figure 2.1: Database: effective indices and scattering matrices of 220 nm-thick SOI strips with widths ranging from 0.4-12µm.

Since the main motivation of the proposed method is to make a standard EME faster and more efficient for optimization, the first goal was to eliminate the optical computations being recalculated each time. In doing so, due to the widespread availability of the devices that can be manufactured, we focused on 220 nm-thick adiabatically varying strip SOI platforms and simulations were performed at $\lambda = 1550nm$ up to a max of 25 eigenmodes ($N_{modes} = 25$). It is important to note that this limit is more than enough in terms of a maximum number of guided modes that can be supported by the widest SOI strip in the database. This might be seen as an overload hindering the EME performance by requiring larger S_{mat}s. However, these simulations also consider the coupling coming from the unguided modes; by tracking these modes, they ensure sufficient spatial resolution [Gallagher and Felici, 2003]. If a database is realized, such a perspective would eventually allow us to simulate a large class of devices using only an array of waveguide widths. As these control points (C_{widths}) will govern the corresponding transverse waveguide geometry, they shall directly control the device's performance. As only the widths determine the resulting N_{eff} & S_{mat}, a database width list (W_{list}) should index the database, as sketched in Figure 2.1. Considering several devices within conventional footprints in the literature, the respective W_{list} range can be settled as 0.4-12µm.

The first question to understand before database creation was where precisely the eigenmodes are solved in an EME Cell. Let's consider W_{cell} is fixed through the cell so that eigenmodes propagate through a constant optical medium; N_{eff} could be easily assigned to the W_{cell}. Likewise, if the width is only linearly increasing or decreasing through the cell, eigenmodes are solved approximately at the centre of each cell; in that case, N_{eff} could be easily assigned to the arithmetic mean of the widths of the cell boundaries. However, we will be working on arbitrary geometries drawn by cubic polynomials [SciPy, 2024] consisting of complex narrowing or widening width profiles. As these geometries are polynomials with sufficient cell resolution, the optical path in an EME cell can be approximated as linearly changing width profiles without loss of generality. Since the recipe for the linear regions is explained above, where N_{eff}s are solved in any accurately sampled geometry is precisely known. As the possible device geometries are restricted to the symmetric ones along the propagation direction, these regions can be represented as isosceles trapezoid-shaped strips visualized in Figure 2.2.

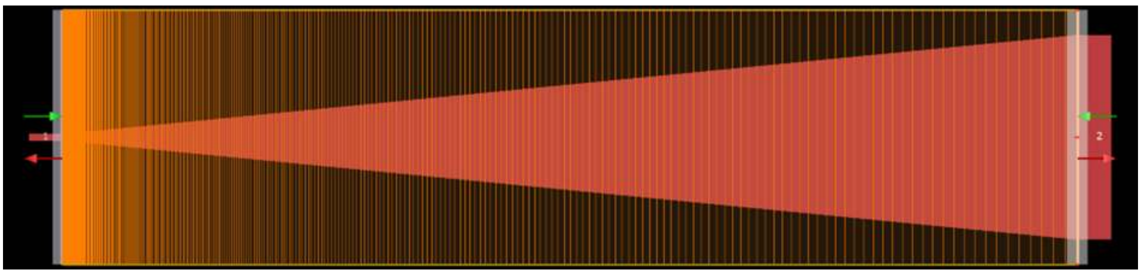

Figure 2.2: The EME simulation layout for database extraction. The computational requirements for this process are the same as those required for a typical EME simulation, which takes about 100 minutes on a desktop computer.

Before forming the respective database layout, the cell resolution aspect is solved by arranging the W_{list}. Typically, linearly spaced widths would be convenient to guarantee sampling of the device in necessarily finer sections; however, this would require a lengthy W_{list} directly affecting the performance as it would essentially result in oversampling of the device geometry. At this point, physical intuition comes to our aid; eigenmodes' EM field profiles tend to change much faster in narrower widths with respect to wide interfaces. In order to exploit this dynamic, a logarithmically spaced W_{list} is suggested; this means narrow widths will be represented with finer sections while wider widths are sampled coarser. Such an approach would keep the number of widths at an optimal limit while providing physical accuracy.

As noticed, this layout calculates S_{mat}s representing increasing width transitions; however, arbitrary geometries will definitely involve decreasing widths. Thus, each width must index two different S_{mat} together with N_{eff}. Revisiting the S_{mat} definition in Equation 2.1, the corresponding S_{mat} for the narrowing sections is calculated in Equation 2.3. With that being added, the recipe for the database is completed.

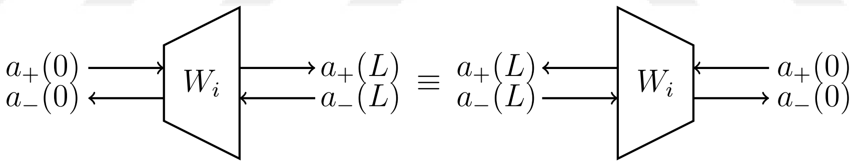

$$\begin{bmatrix} a_-(0) \\ a_+(L) \end{bmatrix} = \begin{bmatrix} S_{11} & S_{12} \\ S_{21} & S_{22} \end{bmatrix} \begin{bmatrix} a_+(0) \\ a_-(L) \end{bmatrix} \equiv \begin{bmatrix} a_+(L) \\ a_-(0) \end{bmatrix} = \begin{bmatrix} S_{22} & S_{21} \\ S_{12} & S_{11} \end{bmatrix} \begin{bmatrix} a_-(L) \\ a_+(0) \end{bmatrix}$$

$$S_{mat,increasing} = \begin{bmatrix} S_{11} & S_{12} \\ S_{21} & S_{22} \end{bmatrix} \qquad S_{mat,decreasing} = \begin{bmatrix} S_{22} & S_{21} \\ S_{12} & S_{11} \end{bmatrix} \tag{2.3}$$

Database extraction is performed with a single Lumerical EME simulation. The Isosceles trapezoid-shaped waveguide is divided with logarithmical spacing into EME cells with a spatial grid resolution of 10 nm. As the W_{list} size determines the resolution of the database, it will directly affect how any waveguide is sampled. An abundance of database widths would require more computational resources for simulation, while the lack of resolution could compromise the physical accuracy;

therefore, finding a balance between them is crucial. First, the database width range was divided into 1200 spaced widths; later, this set size was gradually reduced. Thus, the results generated with different database set sizes could be compared with FDTD results, as displayed in Figure 2.3. Accordingly, 300 logarithmically spaced widths were chosen for an optimal set size. In the end, the database is formed as: 300-length array W_{list}, 300*N_{modes}-sized 2D-matrix N_{eff} and 299*$(2N_{modes})$*$(2N_{modes})$-sized 3D-matrix S_{mat}.

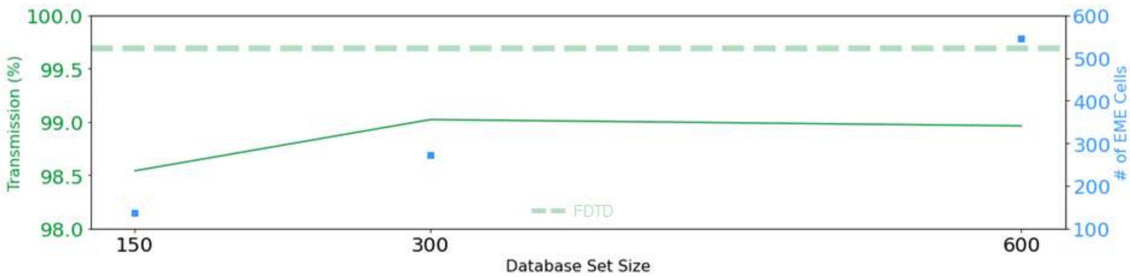

Figure 2.3: Decision on the database: a reference taper is simulated with differently sized databases. The number of simulation cells increases with the W_{list}'s resolution, but the transmission result converges, indicating a possible trade-off between optical accuracy and computational efficiency.

2.3 Geometry Discretization

Nonlinearly-spaced transverse slices must now represent a device according to the W_{list}. The proposed EME method should take C_{widths} as input and then interpolate them with cubic splines [SciPy, 2024] to sample the geometry as an order of W_{list} widths along the propagation direction. In the EME optimization pipeline, W_{input}, W_{output}, L_{device} and $N_{C_{widths}}$ control the input of the optimizer. Besides the imposed database width range on W_{input} and W_{output}, these parameters are flexible.

Discretization operation is designed to approximate geometry's actual widths as W_{list}. In order to do that, C_{widths} should be handled carefully, as the resolution will play an important role one more time. The interpolation's resolution will determine its accuracy as there will be a conformal mapping between the W_{list} and C_{widths}.

After C_{widths} is created, cubic spline interpolation calculates the polynomial coefficients; then, they are turned into an upsampled array under a specific resolution. The level of the upsampling determines which width values are stored in the geometry array. Besides, possible differences between stored neighbouring widths must be greater than the W_{list} deviations to approximate the array to the closest points possible.

Practically, a fixed resolution could be determined to solve such a problem; however, this approach might lead to oversampling of the geometry, increasing the complexity. To propose a geometry-specific solution, the array interpolated with increasing resolution is approximated to W_{list} until it remains stationary. In a while loop, starting with a fixed resolution, the array's resolution is multiplied, and the interpolation is discretized in each step. As the count of approximated widths converges, the optimal upsampling is determined dynamically. Therewith, each value of the array represents the actual widths along the propagation, and the array index maps their propagation-axis location, i.e. $array[first] = W_{L=0}$ and $array[last] = W_{L=L_{device}}$.

The sufficiently sampled geometry is approximated by rounding the geometry array. Since the W_{list} are logarithmically spaced, their logarithm is spaced linearly; therefore, the logarithm of the geometry array is used for rounding. After this step, each value of the array is mapped in terms of W_{list} indices, creating an integer array. Naturally, this result will accumulate some sections with repeating index values, meaning the width remains constant according to the database. Since their indices are related to their location in the device geometry, by taking the difference, their length is determined. Consequently, an ordered sequence of corresponding W_{list} and their length (L_{cell}) pairs are extracted, as visualized in Figure 2.4. This dynamic mapping, in contrast to fixed uniform sampling, segments fast-varying width regions frequently along the propagation axis, improving the physical accuracy while avoiding computational complexity. Also, it's worth mentioning that, even though this conformal representation depends on the spacing of the W_{list} (linear, polynomial, etc.), it offers an alternative to placing the EME cells on the waveguide. Therefore, the simulation will be almost invariant under different W_{list} spacings with sufficient resolution.

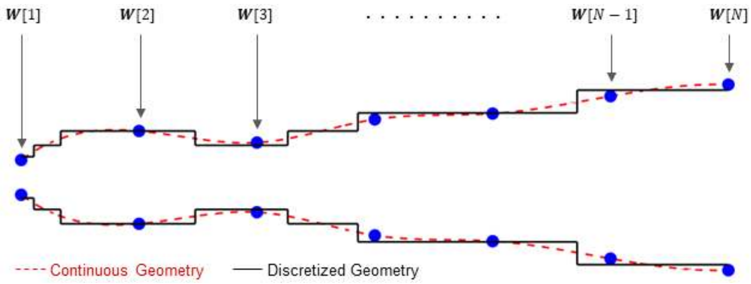

Figure 2.4: Interpolation of C_{widths} and the discrete representation of the device geometry. Each W[i] depicts a width from the W_{list} and the length of each step in the black solid line denotes the respective L_{cell}.

2.4 Simulation

After the discretization, the arbitrary geometry is divided into cells according to L_{cell} array as visualized in Figure 2.5. As in traditional EME simulation, the necessary optical information needs to be calculated. Using the L_{cell} with the corresponding N_{eff}, P_{mat}s are constructed as $2N_{modes}$*$2N_{modes}$ matrices according to Equation 2.2. Then, keeping track of the W_{cell}'s deviation, $S_{mat,increasing}$ and $S_{mat,decreasing}$ are collected from the database. In the end, optical data for a N_{cell}-sectioned device compromises of N_{cell}*$2N_{modes}$*$2N_{modes}$ P_{mat}s and $(N_{cell}-1)$*$2N_{modes}$*$2N_{modes}$ S_{mat}s. Processing this information will heavily depend on the matrix operation conducted on these batches of matrices. To efficiently deal with them in the GPU, their memory allocation is made as a single $(2*N_{cell}-1)$*$2N_{modes}$*$2N_{modes}$ $PyTorch$ tensor.

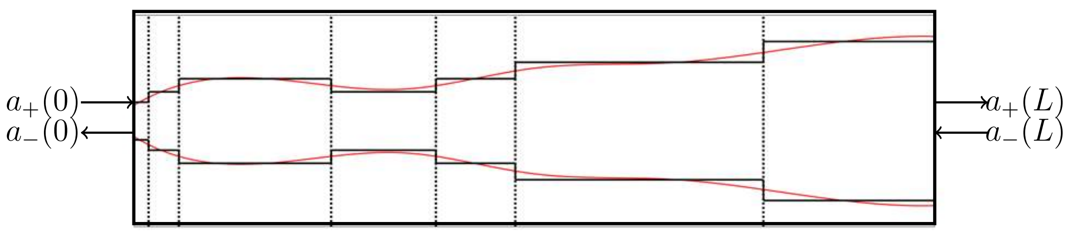

Figure 2.5: How the ROMEO interprets the respective structure in Figure 2.4: dashed lines indicate separate EME cells.

2.4.1 Cascading Scatter Matrices

Since the retrieved optical information of each cell is compared with the actual EME simulation data, it's already known that the proposed method is accurate except for the Overall Scatter Matrix. Unfortunately, the question of how the EME software calculates this matrix remains a mystery; therefore, some educated guesses had to be made for this operation.

$$\begin{bmatrix} a_+(L) \\ a_-(L) \end{bmatrix} = \begin{bmatrix} T_{11} & T_{12} \\ T_{21} & T_{22} \end{bmatrix} \begin{bmatrix} a_+(0) \\ a_-(0) \end{bmatrix} \tag{2.4}$$

Considering the fundamental difference between a S_{mat} (Equation 2.1) and a T_{mat}(transfer matrix) in Equation 2.4, they both keep the scattering information of the optical interface; however, they have slightly different mappings. An S_{mat} maps the incoming eigenmodes to outgoing eigenmodes from the waveguide, while T_{mat} maps the bi-directional input eigenmodes to output eigenmodes in the propagation direction. Supposing the Overall Scatter Matrix calculation should be performed by cascading simulation cells propagation-wise, the T_{mat} method could be the solution.

$$T_{mat} = \begin{bmatrix} S_{21} - S_{22}S_{12}^{-1}S_{11} & S_{22}S_{12}^{-1} \\ -S_{12}^{-1}S_{11} & S_{12}^{-1} \end{bmatrix}, S_{mat} = \begin{bmatrix} -T_{22}^{-1}T_{21} & T_{22}^{-1} \\ T_{11} - T_{12}T_{22}^{-1}T_{21} & T_{12}T_{22}^{-1} \end{bmatrix} \tag{2.5}$$

According to this method, all the matrices should be translated into T_{mat} as prescribed in the Equation 2.5, then multiplied and translated back into S_{mat}. The first tests on relatively less-N_{cell} geometries were promising; however, the Overall Scatter Matrices tend to blow up as the N_{cell} increases. Since these optical interfaces should conserve eigenmodes' energy, the T_{mat} method evidently failed. Carefully analyzing the possible reasons, it's discovered that some S_{mat}s in the database have singular transmission blocks, meaning S_{12}^{-1}s are not defined.

The way the database is constructed leads to minor variations in N_{eff}; therefore, the eigenmodes are inherently expected to experience minimal mode-mismatch as possible as they propagate through consecutive database widths. As seen in Figure 2.6, most of the eigenmodes preserve themselves as they propagate through the

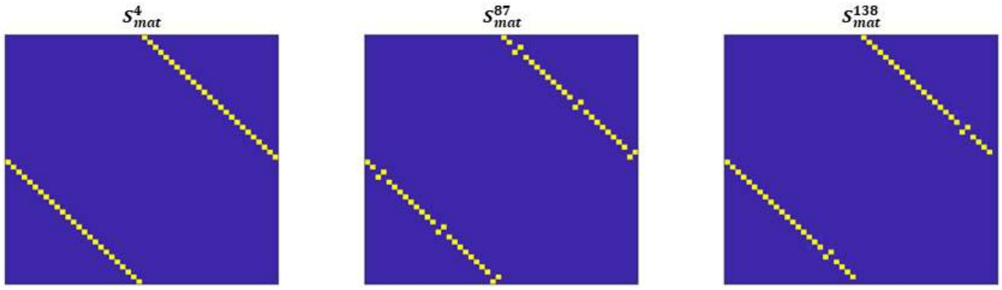

Figure 2.6: Selected S_{mat}s from the database: as expected, transmission blocks of each matrix are close to identity, and the 25^{th} mode is coupled to the higher-order for a few widths.

cell boundaries; however, sometimes they couple to higher-order modes. Although this is not a problem in most cases, coupling to the 26^{th} mode causes singularity, as exemplified in the figure's last S_{mat}. Since the EME solver computes the eigenmodes for only 25 modes, coupling to the 26^{th} mode takes away all the power of 25^{th} mode. By changing the total number of modes solved, the problem was tried to be avoided, but this was not possible with such a diverse width range.

$$\begin{aligned}
\mathbf{S^{AB}} = S^A \times S^B &= \begin{bmatrix} S_{11}^{AB} & S_{12}^{AB} \\ S_{21}^{AB} & S_{22}^{AB} \end{bmatrix} = \begin{bmatrix} S_{11}^{A} & S_{12}^{A} \\ S_{21}^{A} & S_{22}^{A} \end{bmatrix} \begin{bmatrix} S_{11}^{B} & S_{12}^{B} \\ S_{21}^{B} & S_{22}^{B} \end{bmatrix} \\
&= \begin{bmatrix} S_{11}^{A} + S_{12}^{A}[I - S_{11}^{B}S_{22}^{A}]^{-1}S_{11}^{B}S_{21}^{A} & S_{12}^{A}[I - S_{11}^{B}S_{22}^{A}]^{-1}S_{12}^{B} \\ S_{21}^{B}[I - S_{22}^{A}S_{11}^{B}]^{-1}S_{21}^{A} & S_{22}^{B} + S_{21}^{B}[I - S_{22}^{A}S_{11}^{B}]^{-1}S_{22}^{A}S_{12}^{B} \end{bmatrix}
\end{aligned} \tag{2.6}$$

Such a setback brought the S_{mat} notation back since there was no feasible way to eliminate the singular transmission blocks. At this point, Redheffer Star Product had come to our rescue [Redheffer, 1961]. This operation, explained in Equation 2.6, combines the two consecutive linear scatterers S^A & S^B and doesn't require S_{12}^{-1} thus not introducing any singularity. The Overall Scatter Matrix is then calculated in a for loop, where each matrix of the tensor is cascaded on GPU with this product in a linear order and compared with a Lumerical EME simulation set up with the same mesh accuracy, total time accelerated from ~100 minutes to 533ms, enabling four orders of magnitude speed-up.

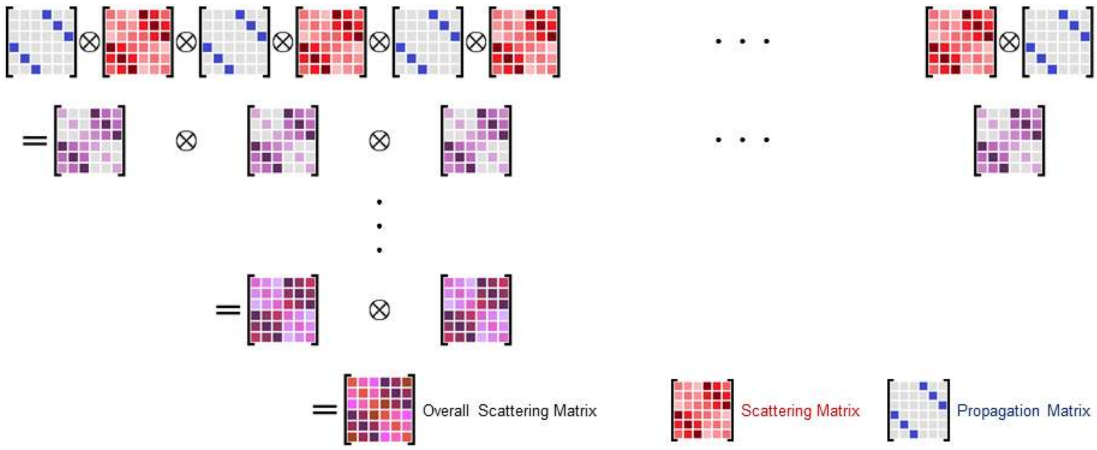

Figure 2.7: Calculation of the Overall Scatter Matrix: parallel multiplication of the respective P_{mat} & S_{mat} under the star product.

2.5 Improving Simulation

2.5.1 Parallelization

Since the cascading method is associative, consecutive matrices' products can be calculated synchronously. Using a Cuda accelerator with the GPU, parallel and asynchronous computational mechanisms could be exercised on our tensor, where each matrix of the batch is multiplied in $log_2(N_{cell})$ parallel steps, as symbolized in Figure 2.7, lasting around 50ms introducing x10 acceleration. As the database is formed on high spatial resolution and the respective optical calculations are entirely vectorial, the proposed simulation preserves the physical accuracy while maintaining 3-dimensionality despite the introduced computational efficiency.

2.5.2 Neumann Approximation

Although this star product consists of matrix multiplications, the calculation of inverses $[I - S_{11}^B S_{22}^A]^{-1}$ and $[I - S_{22}^A S_{11}^B]^{-1}$ are much more computationally intensive. However, the width resolution of the database might open up a window of improvement. Since S_{mat}s include minimal mode-mismatch as mentioned in 2.4.1, the reflection blocks S_{11} and S_{22} are nearly zero in magnitude, just like their product. Hence, Neumann approximation [Stewart, 1998] can be used to estimate these inverses as $(I - S)^{-1} \approx \Sigma_{k=0}^{K} S^k$ (K: expansion order). Comparisons showed that using only four terms (K=3) would be enough to approximate the products; with these improvements, the simulation becomes 25% faster.

Combined with the data-driven approach, outlined improvements accelerate the conventional EME at many orders of magnitude, illustrated by the comparative chart in Figure 2.8. This comparison demonstrates the time complexity of the major EME steps: discretization of the geometry, calculation of the tensor consisting of S_{mat}s & P_{mat}s and the above-explained star product operations. Separate columns of each update indicate the computational weight of the respective step. For the traditional EME time reference, an example device is simulated within a 15μm x 3μm cross-sectional simulation window using 300 EME cells in Lumerical [Lumerical, 2024]. This operation lasts around 100 minutes, and it is evident that replacing eigenmode calculations with pre-computed optical information introduces the predominant enhancement of the method. The data-driven simulation lasts around 533 ms, enabling over 11000x speed-up while maintaining the accuracy. Since discretization and the data retrieval steps are relatively straightforward algorithms, they couldn't be structured more efficiently; only the product step remains to have room for improvement. As explained above, parallelization and Neumann approximation introduced the final boost to the product, enabling an additional 10x speed-up, resulting in as short as 41.2 ms simulation times. Compilation of these improvements accelerates the single-device simulation over five orders of magnitude for all devices that will be demonstrated. As mentioned before, the common database can carry out the simulations of waveguides with continuous geometries. It is reused to simulate the existing device with modified C_{widths} or to simulate entirely new devices. Therefore, the computational resources to create the database are independent of the reported device simulation times. The timeframe analysis is conducted on a single-core Intel 9700 CPU with a Tesla V100 GPU through Google Colaboratory Cloud service.

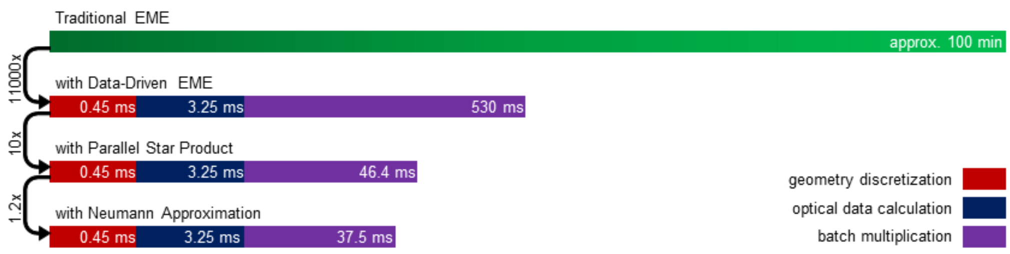

Figure 2.8: Time evolvement of the method: From 100-min-long traditional EME to 41.2-ms-long data-driven EME with the proposed improvements, representing a five orders of magnitude speed-up.

2.6 Optimization

Achieving physically accurate and time-efficient simulations of the device transmission characteristics has significant implications for the inverse design of high-performance integrated photonic components; it introduces previously elusive opportunities for iterative device optimization networks. If the optimization aspect is appropriately constructed, this pipeline can efficiently design broadband and compact devices for many photonics applications.

2.6.1 Suitable Optimization Network

First, let's define the optimization problem in the simplest form possible: With the given design parameters, the network should find the optimal C_{widths} array so that the geometry they sample satisfies the desired transmission profile. Input design parameters are W_{input}, W_{output}, L_{device} and $N_{C_{widths}}$ and they determine the input vector C_{widths}. Since the Overall Scatter Matrix computed by our EME already holds all the necessary information, values extracted from this $2N_{modes} * 2N_{modes}$ matrix will be the output value. As the C_{widths} controls the order of matrices to be multiplied, the optimization problem can be summarized as finding the optimal matrix sequence whose product gives the desired Overall Scatter Matrix. As it is understood, this nonlinear problem is hard to define in terms of mathematics; therefore, any gradient-based approach would require an excessive number of matrix products, increasing the complexity. In this regard, a gradient-free approach would be more convenient for our scheme.

If the optimization has a global search, C_{widths} vector might overshoot the W_{list} range during its evolution. This wouldn't pose a problem since the whole geometry will be approximated to W_{list}; however, it might lead to inaccurate sampling of the device geometry. Consequently, a bounded local search might keep the updating C_{widths} in range. Considering these aspects, the constrained COBYLA algorithm [Powell, 2007] is chosen to be implemented on an open-source NLopt network [NLopt, 2024].

2.6.2 Geometrical Constraints

Several constraints are also imposed on the C_{widths} as 1^{st} derivative ($\frac{dw(z)}{dz}$) and radius of curvature (κ). For the sake of minimizing the excitation of higher-order modes, $\frac{dw(z)}{dz}$ constraint is included to prevent abrupt deviations throughout the waveguide form. Besides, for constructing fabrication-compatible waveguides, the κ constraint, as explained in Equation 2.7, is also incorporated in the optimizer. Both constraints are defined as penalty functions so that if they remain below their respective thresholds upon their optimization, a smooth and fabrication-compatible device is realized.

$$\kappa = max \left| \frac{y''}{(1+y'^2)^{\frac{3}{2}}} \right|, where\ y : interpolated(C_{widths}), y' = \frac{dy}{dx}, y'' = \frac{d^2y}{dx^2} \quad (2.7)$$

2.6.3 Broadband Optimization

From here on, all the necessary steps for realizing an optimizer have been efficiently streamlined and named ROMEO. It can design various structures with flexible parameters simulated on a single transmission wavelength. However, it's not still guaranteed that the optimized devices can show state-of-the-art performance metrics over broadband. For this purpose, additional EME Databases calculated at $\lambda = 1500nm$ and $\lambda = 1600nm$ are integrated into the ROMEO framework. At any time, a device can simultaneously be simulated at multiple wavelengths, i.e.

1500nm, 1550nm, and 1600nm, enabling it to be designed over a band instead of a single wavelength.

2.6.4 Optimizer Convergence under Different Initial Conditions

As with many optimization frameworks, the initial guess directly affects the convergence to the transmission goal and the final device performance. For all of the devices to be studied, 15 different optimizations are implemented on random initial guesses up to a maximum of 200 iterations, as reported in Figure 2.9.

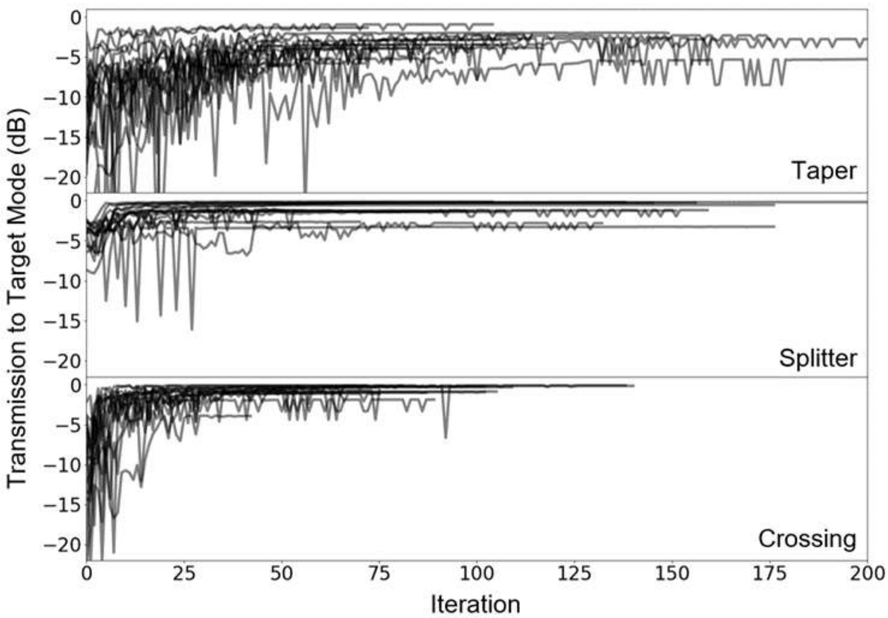

Figure 2.9: Optimizer convergence for all discussed devices under different starting geometries. ROMEO is generally capable of improving the transmission regardless of the initialization.

These transmission curves reveal that the objective function of most devices can be significantly improved regardless of their initial C_{widths}. Also, some optimizations plateau after the first 50-100 iterations, confining into local extrema, yielding inadequate performance metrics. Below 10 seconds, the optimization typically reaches 100 iterations, after which the designer can certainly evaluate the convergence of the device's objective. Such a performance becomes possible by the improvements mentioned in Figure 2.8; however, these may not guarantee the objective convergence of particular unfavourable initial geometries. This well-documented phenomenon is associated with the optimizer's skill, rather than ROMEO, to effectively search for the optimal solution starting from a poor initialization in a multi-dimensional objective space [Mishkin and Matas, 2016, Sutskever et al., 2013]. Employing "multi-start" optimizations to search different localities of the objective's topology more thoroughly and increase the likelihood of a more optimal solution is a common practice to mitigate this phenomenon. Additionally, a possible approximate solution or a physically motivated guess, like a linear form in Figure 3.1, Figure 4.1 and Figure 5.1 can provide beneficial initial conditions for the search of an ideal solution.

2.6.5 Hyperparameter Tuning

The final performance of the optimized device may not satisfy the application-specific target as can be expected from an optimization problem; however, it might be overcome by tuning the hyperparameters. Having fixed the W_{input} & W_{output} for these three device classes to be discussed, L_{device}, $N_{C_{widths}}$ and geometrical constraints (2.6.2) are the prominent hyperparameters. Starting with the L_{device}, the underlying eigenmode dynamics would provide educated guesses for the device lengths so that optimization takes place in the design space of more physically favourable device options [Michaels et al., 2020, Johnson et al., 2020]. Also, $N_{C_{widths}}$ might be tuned to reach better devices; however, there might not be a direct correlation between this number and how the optimization concludes [De la Cruz-Coronado et al., 2020]. Different thresholds for geometrical constraints can be specified in a reasonable range, or different optimizer methods can be implemented to address this challenge. ROMEO's computational efficiency makes it feasible to perform these optimizations while tuning various hyperparameters.

The following sections demonstrate ROMEO's capability to optimize nanophotonic devices on a waveguide taper, a power splitter, and a waveguide crossing. Furthermore, its potential to design 1×3, 1×4, and 2×2 couplers will be discussed to show ROMEO's future applicability to a new set of various devices.

Chapter 3

DESIGN OF A WAVEGUIDE TAPER

3.1 Design & Optimization

ROMEO's capabilities are first demonstrated through a waveguide taper design. Such devices frequently function as transition components, as spot-size converters, for nanophotonic edge and grating couplers. An interpolation of 30 optimizable widths, C_{widths} as denoted by green dots, represents the taper in Figure 3.1 through a propagation length of 30 μm. The device is laterally symmetric, and the input and output waveguide widths, specified by the red dots, are fixed as $W_{input} = 500nm$ & $W_{output} = 9\mu m$, which can be arbitrarily determined for desired optical functionalities.

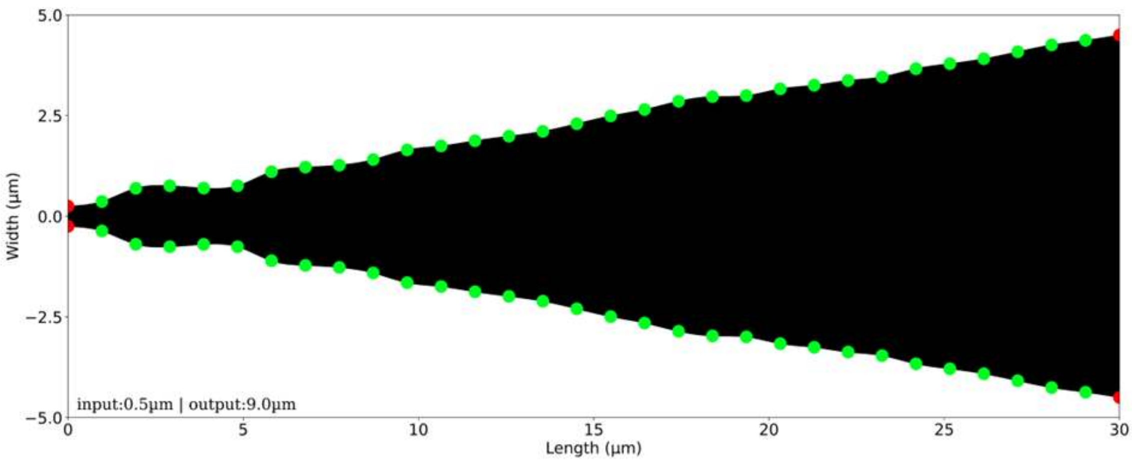

Figure 3.1: Optimized waveguide taper geometry with 30 optimizable C_{widths}, for a 30 μm-long device.

ROMEO evaluates this taper's Overall Scatter Matrix as C_{widths}'s function, computing complex mode-to-mode amplitude coefficients for all eigenmodes. For the sake of simplicity, the input mode is determined as the fundamental TE mode of the input plane of the taper; therefore, the respective transmission vector for a device becomes $T(C_{widths}) = |S_{mat}[N_{modes} : 2 * N_{modes}, 0]|^2$, where each value keeps track of the coupled power to each eigenmode as if FDTD is performed on that structure. In this specific problem, the optimizer is configured to maximize the optical transmission coefficient or minimize the loss, in our case, between fundamental TE modes at the input and output planes. Mathematically, the objective function for this design problem can be constructed in either scalar ($O(C_{widths}) = 1 - T(C_{widths})[0]$) or vectorial ($O(C_{widths}) = |[1\,0\,0 \ldots 0] - T(C_{widths})|$) way. Even though the scalar option is chosen for this case, ROMEO allows both ways to give flexibility to optimization.

The initial guess for C_{widths} is specified with linearly increasing widths starting from the user-specified W_{input} and extending to the W_{output}, as it's a physically motivated starting geometry. The device's objective and constraints progress throughout the optimization process as plotted in Figure 3.2. Throughout the iterations, C_{widths} evolves non-linearly, contrary to fixed analytical or adiabatic representations of tapers [Michaels and Yablonovitch, 2018], gradually arriving towards the 0dB desired transmission. Mathematically speaking, the objective function's topology determines the whole optimization space, and the initialization designates a locality to start. Depending on the chosen algorithm [SciPy, 2024], the algorithm traverses through a specific path by probing possible device geometries. After experiencing numerous fluctuations in 277 iterations, power coupled to the fundamental TE mode at the output of the device is maximized to 99% (-0.0436dB) at the wavelength of λ=1550 nm, with 10^{-5} relative convergence criterion within 18 seconds. Also, it's important to note that the same optimization result can be followed as minimizing the power coupled to the higher-order modes.

In addition to maximizing the overlap between the output field's mode profile and the desired optical output mode, the first derivative, $\frac{dw(z)}{dz} < 2$, and radius of curvature, $\kappa < 1\mu m^{-1}$, constraints are included; and they are plotted in the bottom part of Figure 3.2. Curves demonstrate that iterations may temporarily evolve to geometries violating these constraints to reach the desired transmission objective; however, their constraints ultimately remain well below their thresholds, indicated by dashed lines, ensuring fabrication-compatible smooth layouts.

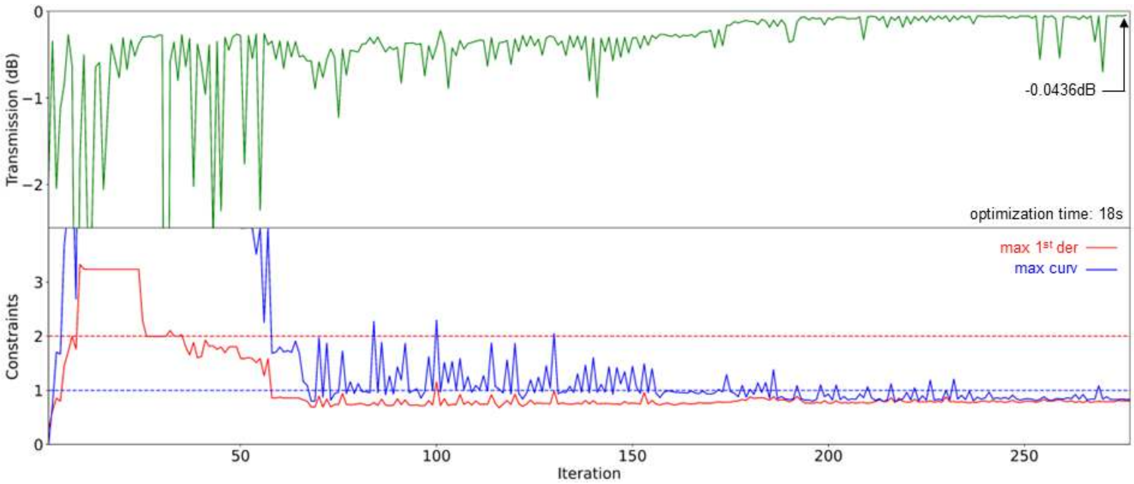

Figure 3.2: Optimization progress: Evolution of the transmission to the fundamental TE mode at the output plane and constraints.

3.2 Discussion of the results

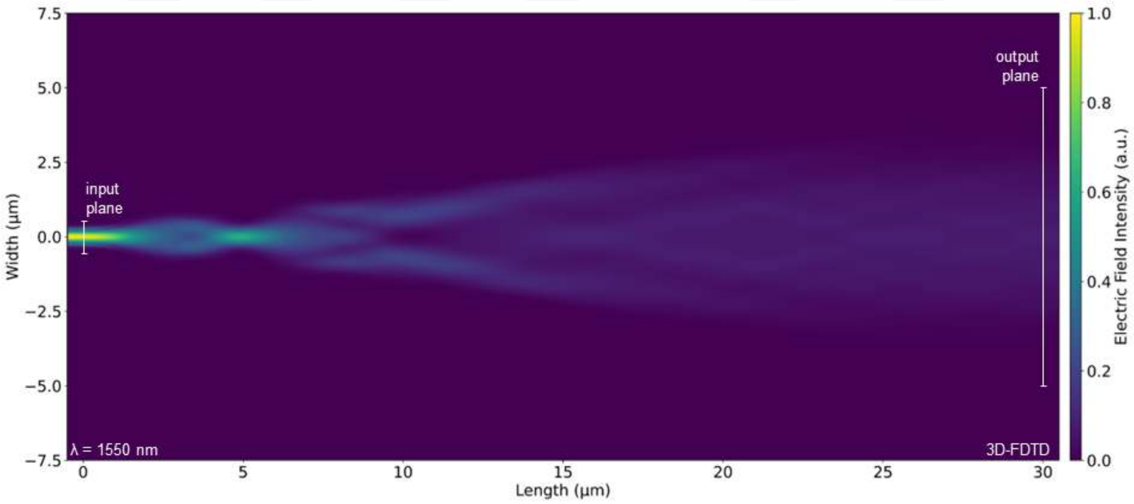

Figure 3.3: 3D-FDTD result displaying the spatial evolution of the input TE mode.

The optimized taper is verified with 3D-FDTD simulations [Lumerical, 2024], given a TE-mode input, and the resulting electric field intensity profile is illustrated in Figure 3.3 where solid lines show the input and output planes. Additionally, using a mode expansion monitor, the output field and the target fundamental TE mode are compared in Figure 3.4. The simulation concluded that 99.7% of the input power is coupled to the fundamental TE mode at the 9-μm-wide output of the device. This evaluation verifies that the much smaller input mode can spatially evolve to the output plane's intensity profile with as minimal interference as possible from higher-order modes, as plotted in Figure 3.5, thus matching the desired fundamental mode profile.

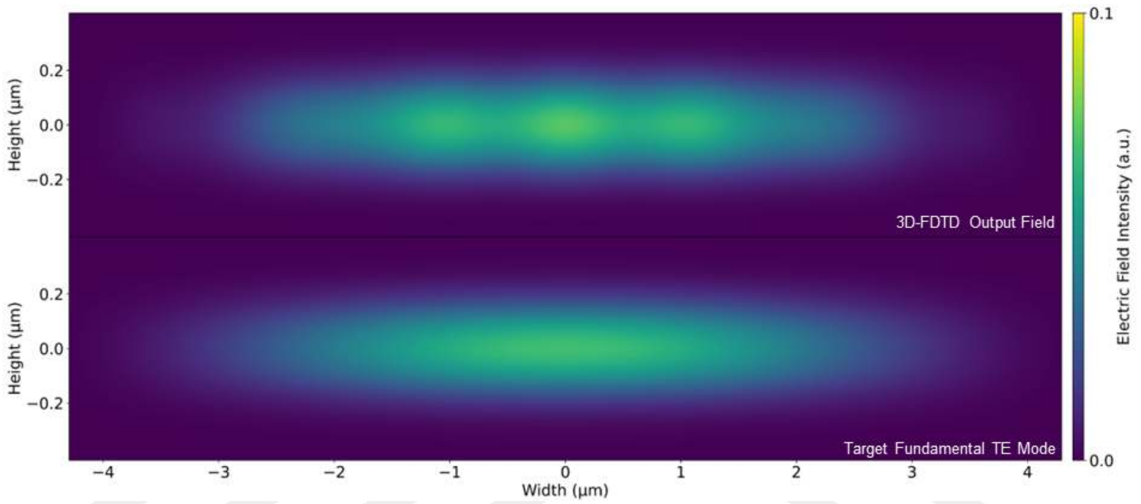

Figure 3.4: 3D-FDTD verifies 99.7% of the input power is coupled to the fundamental TE output mode, showcasing a near-lossless match with this target mode.

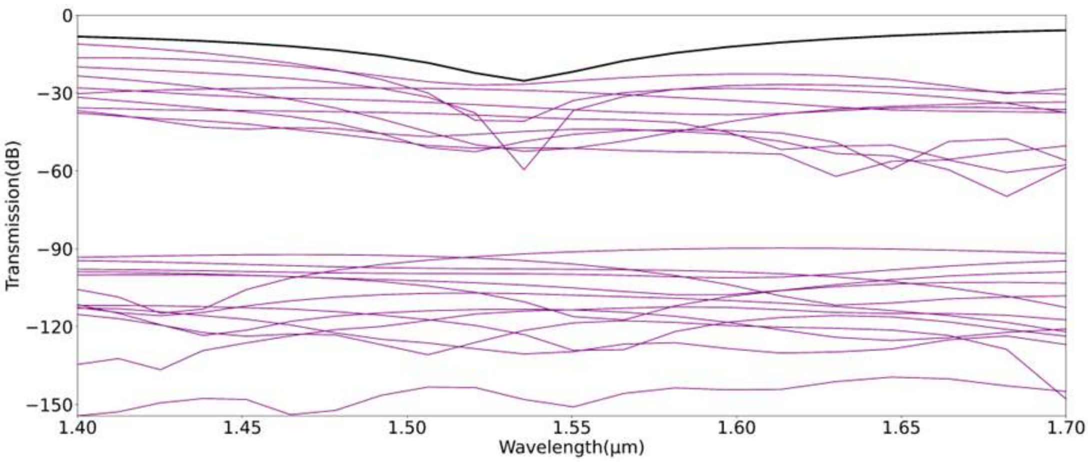

Figure 3.5: Transmission spectra of the higher-order modes: Mode#3 is specified with a thick black curve, and it yields the majority of the 0.3% power coupled to the higher-order modes at the output of the device.

Even though a single wavelength ($\lambda = 1550nm$) is considered to design this taper, it operates with a wide optical bandwidth. Its 1dB bandwidth remains above 250 nm while providing less than 40dB reflection over the entire band, as illustrated by the 3D-FDTD result in Figure 3.6.

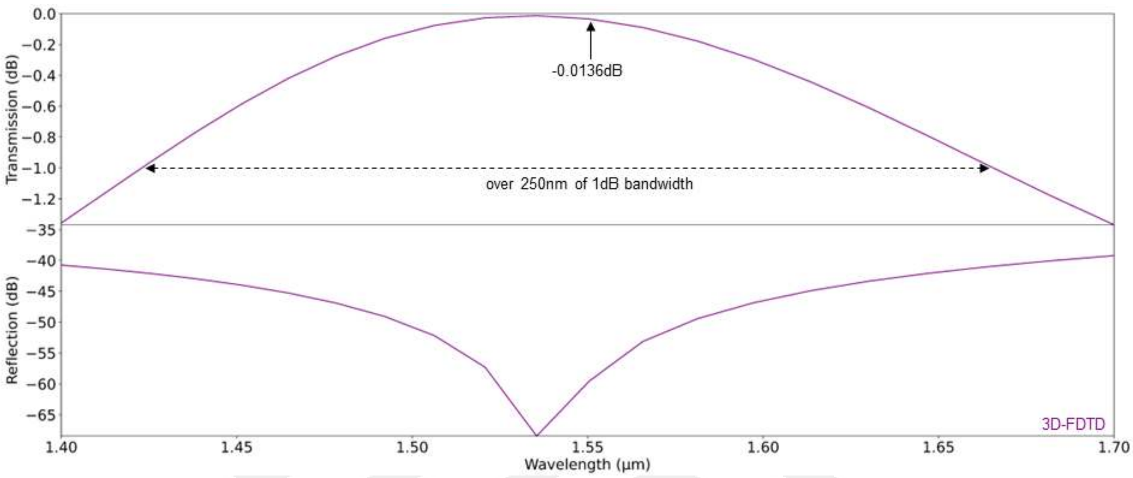

Figure 3.6: Optical spectrum: -0.0136dB transmission at $\lambda = 1550nm$, 1dB bandwidth over 250nm with less than 40dB reflection over the entire band.

In addition to the FDTD verifications, the results of the fabricated device will further elaborate the discussion. For the measurements, hundreds of adiabatic taper pairs are cascaded on a waveguide path between grating couplers, as sketched in Figure A.1. While placing them on the mask, tapers are paired by combining their output planes, and each pair's input & output width become 0.5µm, matching the path width.

The measured power spectrum is analyzed in relation to the power loss introduced by the grating couplers. Transmission per taper is approximated by fitting a line between the measurements in Figure 3.7. At $\lambda = 1550nm$, the taper demonstrates around -0.050dB transmission of the fundamental TE mode. Generalizing this analysis to the entire C-band, the taper's spectrum is compared with the FDTD result, as overlaid in Figure 3.8. Considering that the spectrum is at the mdB level, there is no incompatibility with the FDTD result, and it is close to lossless operation.

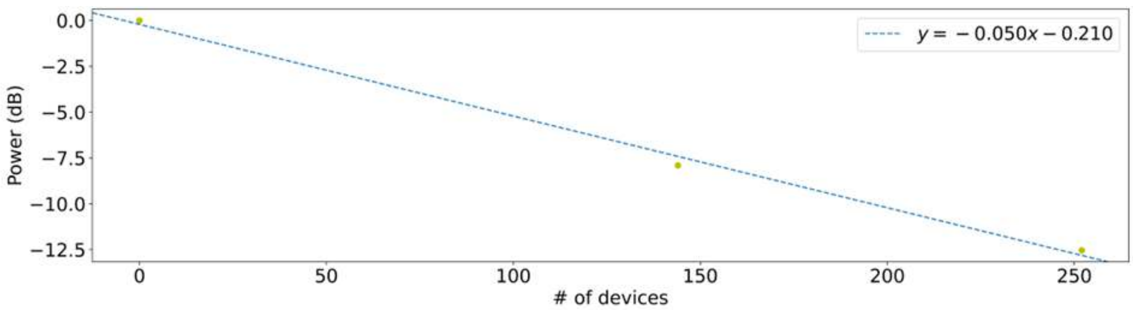

Figure 3.7: Taper transmission: -50mdB at $\lambda = 1550nm$, in contrast to the -14mdB FDTD result.

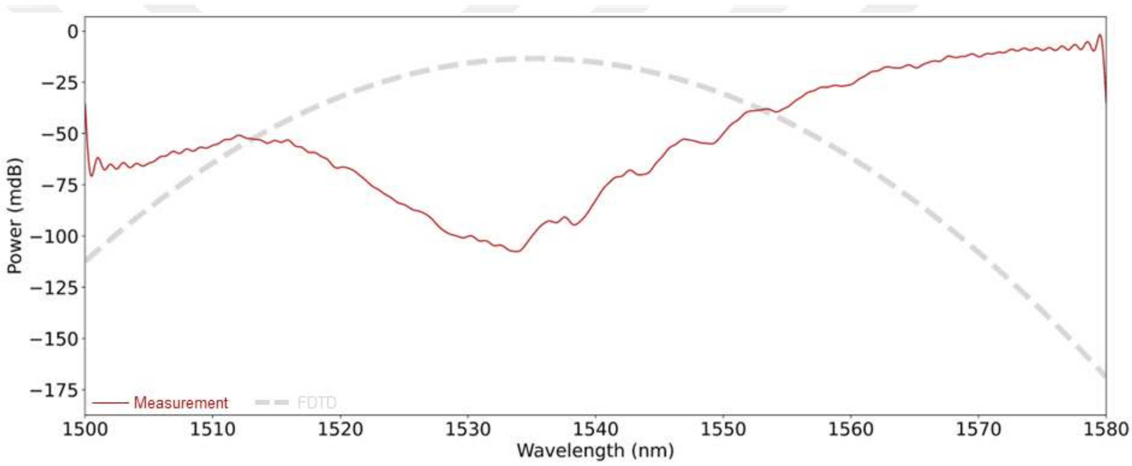

Figure 3.8: Optical spectrum compared with the FDTD spectrum(dashed lines).

Comparing these metrics with the high-performance designs in the literature, as reported in Table 3.1, the optimized device demonstrates consistent power coupling efficiencies in an exceeding operation bandwidth while achieving orders of magnitude faster design times. Also, the proposed network could be modified to achieve coupling to the spatially symmetric higher-order modes for other integrated photonics components like spatial mode converters.

Table 3.1: Comparison of Adiabatic Tapers

Work	Dimensions (μm)	Transmission (mdB)	Thickness (nm)
[Michaels and Yablonovitch, 2018]	L: 18, W: 0.5→9	-41	220
[Sethi et al., 2017]	L: 15, W: 0.5←10	-170	220
[Abdeen et al., 2019]	L: 22, W: 0.5→15	-362	220
[Garza and Sideris, 2023]	L: 18, W: 0.5→6	-288	220
	L: 18, W: 0.5→9	-409	220
this work	L: 30, W: 0.5→9	-50(fab.)/-14(FDTD)	220

These results highlight ROMEO's capabilities to design near-losses, high performance, broadband, fabrication-compatible adiabatic tapers with user-specified W_{input} and W_{output} within thousands of times faster computational time scales compared to conventional methods.

Chapter 4

DESIGN OF A 1×2 POWER SPLITTER

4.1 Design & Optimization

ROMEO framework also offers adaptability to devices with multiple outputs, such as commonly used power splitters; it will be demonstrated through a compact continuous strip 3 dB splitter design. The laterally symmetric device is represented using five optimizable C_{widths} inside a $2 \times 2\mu m^2$ footprint. The initial guess using linearly increasing C_{widths}, as shown in Figure 4.1 which is similar to the initial taper case, formed with $W_{input} = W_{output}s = 500nm$ and 0.2 μm fixed separation between output waveguides.

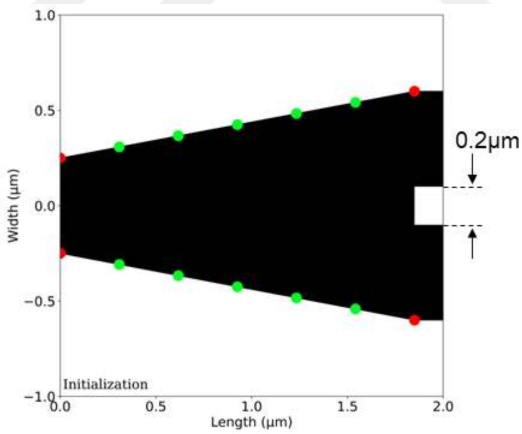

Figure 4.1: Initial 1×2 splitter geometry with 5 optimizable C_{widths}, with a 0.2μm fixed gap between the outputs.

In a 3dB coupler, eigenmodes propagate between the single-waveguide section through the double-waveguide output section, as illustrated in Figure 4.1, thus introducing a discontinuous optical interface. Therefore, unlike the ROMEO database consisting of continuous optical interfaces, the splitter requires an additional S_{mat}

for the 1×2 geometry. Since W_{output} and the gap between them will be fixed, S_{mat} is computed with the respective 2-cell simulation in Figure 4.2. Having completed the missing scattering information, all that remains is to add this matrix to the batch. First, the leading matrices are multiplied just like the taper, and the final splitting matrix is included in the calculation.

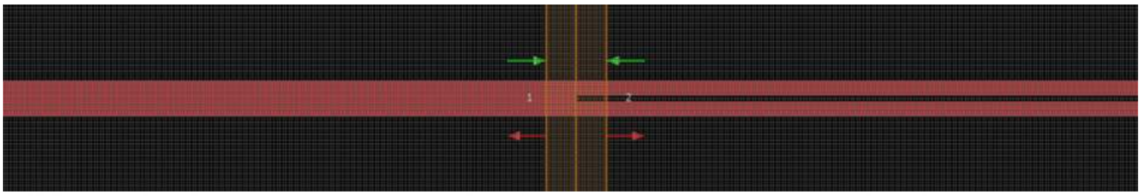

Figure 4.2: The 2-cell EME simulation layout for the respective S_{mat}, representing the optical effect of the output waveguide split.

Throughout the optimization, C_{widths} are updated, and the leading batch of matrices is multiplied with the constant corresponding S_{mat}. For this 1×2 geometry, even and in-phase optical splitting is aimed at its symmetrical output waveguides; therefore, given a TE mode input, the objective function is reconfigured to maximize the transmission between the fundamental TE modes at the input and output planes, similar to the taper example. As before, the device optimization is conducted under the COBYLA algorithm with the constraints $\frac{dw(z)}{dz} < 2$ & $\kappa < 4\mu m^{-1}$. The consequent splitter, depicted in Figure 4.3, fits compactly within the specified footprint even though its peak wideness exceeds the W_{output}, indicating that the bounded optimization works sufficiently. Through 445 iterations within 14 seconds, the final transmission reaches up to 97.1% (-0.1278 dB) between the specified fundamental input and output modes, as plotted in Figure 4.4. During this process, constraints experience variations like the objective function, and they ultimately satisfy their threshold.

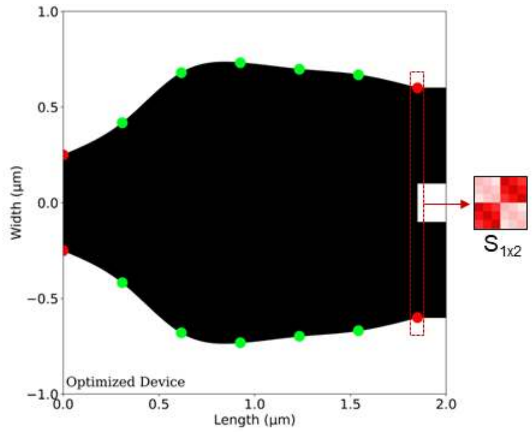

Figure 4.3: Optimized 1×2 splitter geometry inside a $2 \times 2\mu m^2$ footprint, together with the constant S_{mat}, to be multiplied at the output.

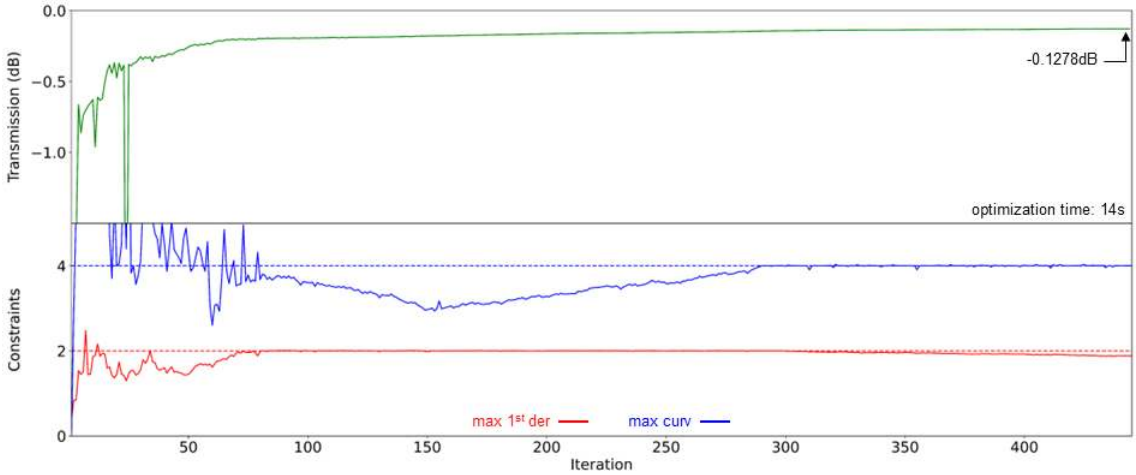

Figure 4.4: Optimization progress: Evolution of the transmission to the fundamental TE mode at the output plane and constraints.

4.2 Discussion of the results

Adding S-bends at the end of the 3dB splitter to separate the device into uncoupled distinct waveguides, the optimized device is verified with 3D-FDTD, whose electric field can be seen in Figure 4.5. The splitter's simulated 0.1355dB excess insertion loss, as demonstrated in Figure 4.6, is consistent with the 3dB couplers designed with similar optimization frameworks and those having mode-evolution-based (adiabatic)

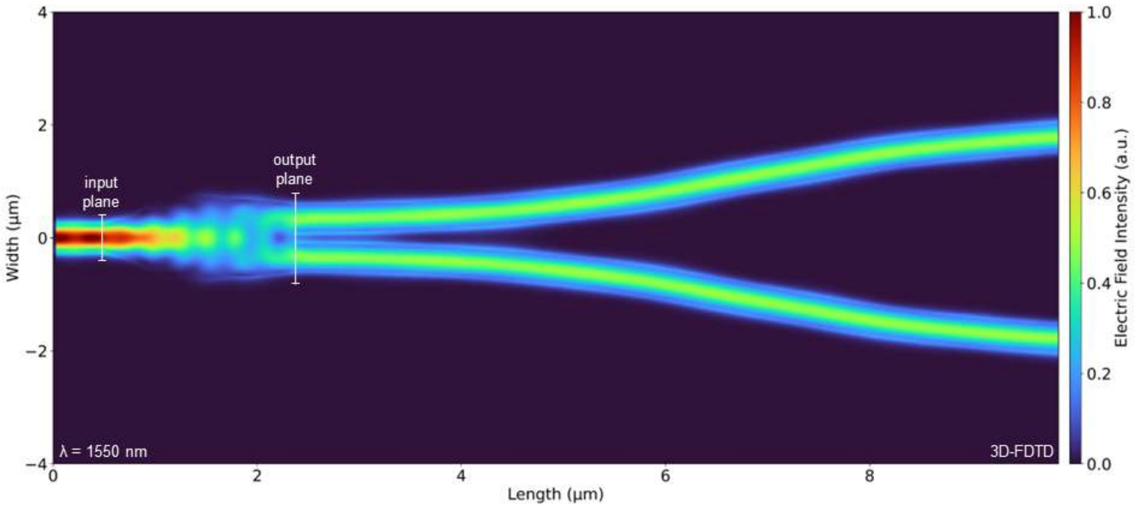

Figure 4.5: 3D-FDTD result exhibits the S-bends' even and in-phase power splitting.

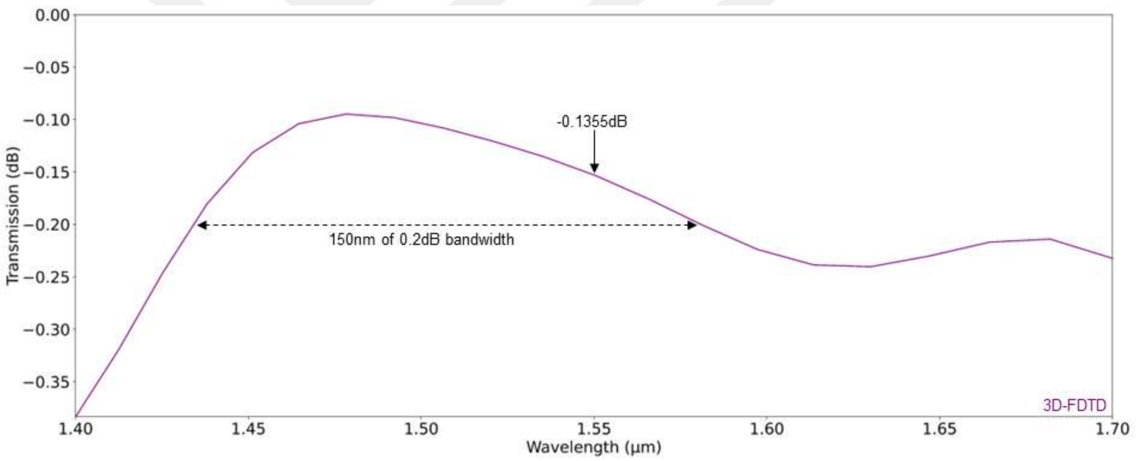

Figure 4.6: Optical spectrum: -0.1355dB transmission at $\lambda = 1550nm$, with 0.2dB bandwidth of over 150 nm.

geometries [Zhang et al., 2013]. The additional loss for over a 150 nm bandwidth remains below 0.2dB, indicating the optimized structure's broadband functionality under high performance. Comparatively, the 1-dB bandwidth extending over 300 nm exceeds many other compact designs demonstrated in Table 4.1. These metrics indicate a close match between the FDTD and ROMEO calculations, suggesting our method's physical accuracy can be extended to a new set of devices with discontinuous interfaces. Moreover, this method brings a wide operational utility to potentially design compact interferometers, including 2×2 couplers or 2x4 (90° hybrid) structures.

Table 4.1: Comparison of 1×2 Splitters

Work	Footprint (μm^2)	Transmission (mdB)	Thickness (nm)
[Garza and Sideris, 2023]	not disclosed	-153	250
[Lalau-Keraly et al., 2013]	2×2, W: 0.5 gap: 0.2	-70	220
[Zhang et al., 2013]	2×1.2, W: 0.5 gap: 0.2	-280 ± 20	220
[Michaels et al., 2020] λ:1310nm	3.94×1.75, W: 0.5 gap: 0.5	-20	220\w 110 partial
[De la Cruz-Coronado et al., 2020]	2×1.5, W: 0.5 gap: 0.2	-60	220
[Nguyen et al., 2019] Tapered Rib Waveguides	L: 19, W: 0.2→0.45 spacing: 0.25	-80	220\w 110 partial
[Lin and Shi, 2019] (asymmetric)	2.32×1.4, W: 0.5 gap: 0.2	-220⟷360 for diff splittings	220
this work	2×2, W: 0.5 gap: 0.2	-83(fab.)/-136(FDTD)	220

Upon examining the works in the table, it can be said that ROMEO's separation of output waveguides with a fixed gap may limit the further optimization of the geometry, which can be addressed by modifying the respective section. The simulation of such a geometry would require an additional database of N_{eff}s & S_{mat}s taken from the split region as a function of both the gap between symmetric output waveguides and their width. Afterwards, the same framework can optimize the single-waveguide and the two-waveguide structures together. Nevertheless, an extension of the database in a multi-variate approach might introduce computational complexity; such a trade-off must be studied compared to time-domain or frequency-domain inverse design-based methods [Hammond et al., 2022, Dasdemir et al., 2023]. Also, the proposed splitting template enables the user to arrange the output waveguides in any application-specific configuration since the ROMEO optimizes the device up to the propagation distance where the waveguides are just split.

The optical response of the splitter is also measured to detail its performance, along with the FDTD simulations. Tens of splitters are paired in units, then cascaded to form an optical path between grating couplers displayed in Figure A.2. Each splitter is aligned with its mirrored counterpart, and the gap between them is populated with split output waveguide strips. These units' input & output width are 0.5μm, in agreement with the path width.

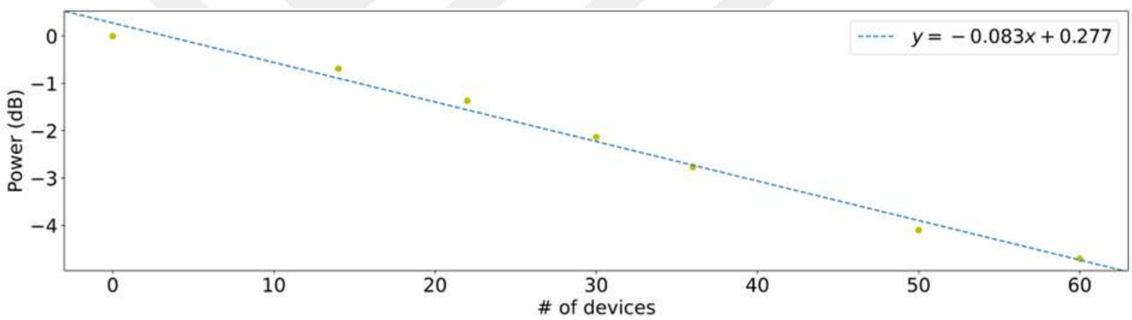

Figure 4.7: Splitter transmission: -83mdB at $\lambda = 1550nm$, in contrast to the -136mdB FDTD result.

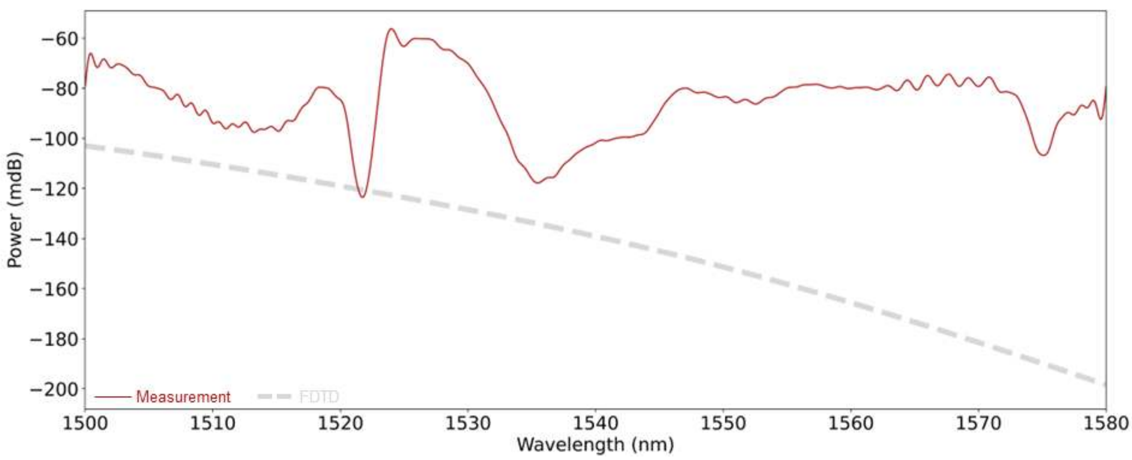

Figure 4.8: Optical spectrum compared with the FDTD spectrum(dashed lines).

Optical power is analyzed with respect to the grating coupler insertion loss. Transmission of each splitter is calculated by the slope of the best-fit line going through the measurements in Figure 4.7. At $\lambda = 1550nm$, the splitter achieves -0.083dB transmission of the fundamental TE mode. Considering the C-band, the splitter's spectrum is plotted, and the FDTD result is overlaid for comparison in Figure 4.8, it's observed that the fabricated device demonstrates a slight improvement in transmission.

Chapter 5

DESIGN OF A WAVEGUIDE CROSSING

5.1 Design & Optimization

Waveguide crossings play a critical role in large-scale photonic systems by allowing optical signals to intersect and cross each other in planar geometries. This section will demonstrate ROMEO's capability to efficiently design low-loss and crosstalk on-chip waveguide crossings on a broad operational bandwidth. The 4-fold centre-symmetric design of the crossing geometry allows itself to be represented by only one of its input waveguides, as their C_{widths} are illustrated in Figure 5.1. Here, the interpolation of four C_{widths} constructs the initial continuous form like the initial guess for the taper, and it is replicated on all ports. To prevent the formation of sharp features for fabrication compatibility, the intersections of waveguide pairs are completed with rounded corner pieces, as depicted in the inset.

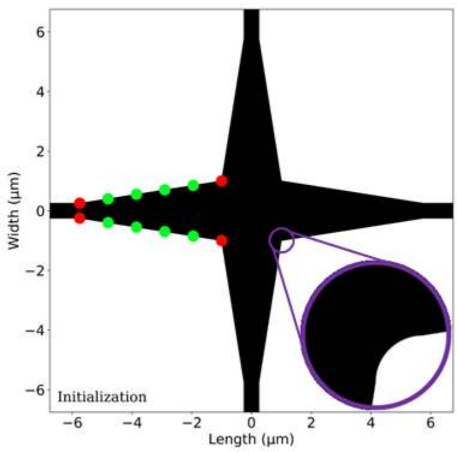

Figure 5.1: Initial waveguide crossing geometry with 4 optimizable C_{widths}, with rounded corners at waveguide intersections.

ROMEO framework has undergone serious modifications to enable it to optimize crossings by considering the fact it's simply a combination of taper sections. Founding a correct recipe, such an implication would allow ROMEO to simulate any symmetric crossing as a sequence of taper simulations. One of the four corners of a crossing, as in the sketch Figure 5.2, consists of 4 regions in propagation order: input taper, rounding piece, upside-down taper, and the half-way to the midpoint. Simulation of the first region is already available in the framework; likewise, the rounding piece simulation becomes available by parametrizing this region as a quarter-circle having an optimizable radius so that the optical response of this region could also contribute to the overall process. However, the upside-down region should be handled carefully because of the constraints of the ROMEO database. Even though C_{widths} sample constantly continuous optical interfaces along the propagation direction, this particular region is parametrized by rotating the input taper by 90°, meaning that it's not guaranteed to have a continuous form with respect to the propagation axis, as exemplified in Figure 5.2. To eliminate this uncertainty, ROMEO calculates this region by pretending it is an isosceles trapezoid, as specified by dashed lines. One might suggest this would lead to a loss of physical accuracy since the geometry is deliberately undersampled into a basic shape; however, introducing potential discontinuous interfaces would cause inaccuracies, so there is a trade-off between them. The last remaining section is simulated with a single P_{mat}, as it has a constant width; in the end, ROMEO calculates these four regions separately and cascades them to obtain the S_{mat} for the first half of the device.

Crossing's underlying mirror symmetry allows ROMEO to simulate the second half of the device just by manipulating the first half's S_{mat} as explained in the Equation 2.3, the symmetric half's response is computed, and then two of them are cascaded to obtain the Overall Scatter Matrix. The objective function is defined to minimize the back reflection and crosstalk at other output ports; therefore, it is inherently specified to maximize the transmission between the fundamental TE modes at the input and output planes along with the same constraints ($\frac{dw(z)}{dz} < 2$ & $\kappa < 4\mu m^{-1}$) under 10^{-5} relative convergence tolerance.

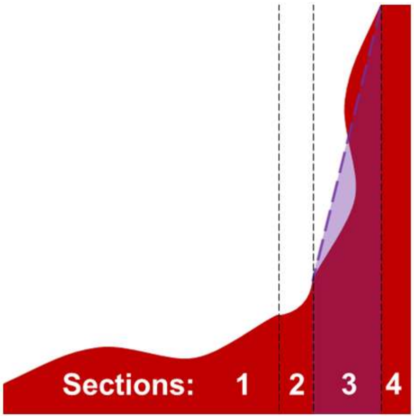

Figure 5.2: A close-up (a quarter of a footprint) of the waveguide crossing in the eyes of ROMEO: Simulations of Sections 1,2 and 4 follow the exact geometry of the device, while in Section 3, the geometry is replaced by the respective linear form shown by the shaded purple.

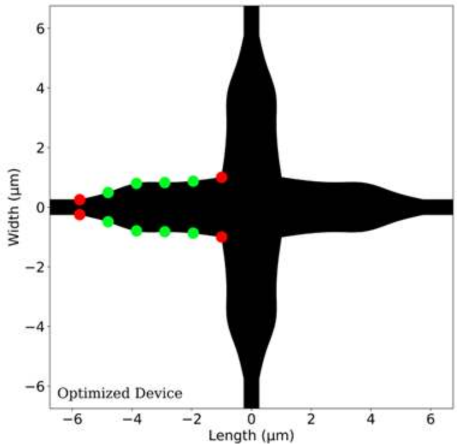

Figure 5.3: Optimized waveguide crossing geometry inside a $12x12\mu m^2$ footprint.

The final optimized crossing, as exhibited in Figure 5.3, fits within a $12x12\mu m^2$ footprint and has 500 nm wide input ports from all sides. Under only 5 seconds, the final transmission reaches -0.0436dB within 49 iterations, as plotted in Figure 5.4. The constraints on waveguide width derivative and curvature are satisfied throughout the entire process, indicating the fabrication compatibility of the resulting structure.

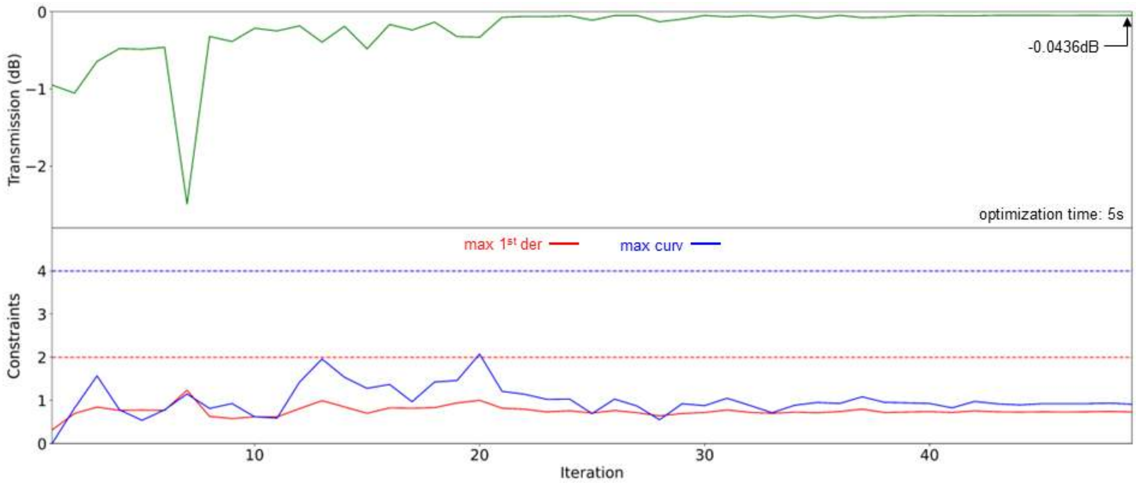

Figure 5.4: Optimization progress: Evolution of the transmission to the fundamental TE mode at the output plane and constraints.

5.2 Discussion of the results

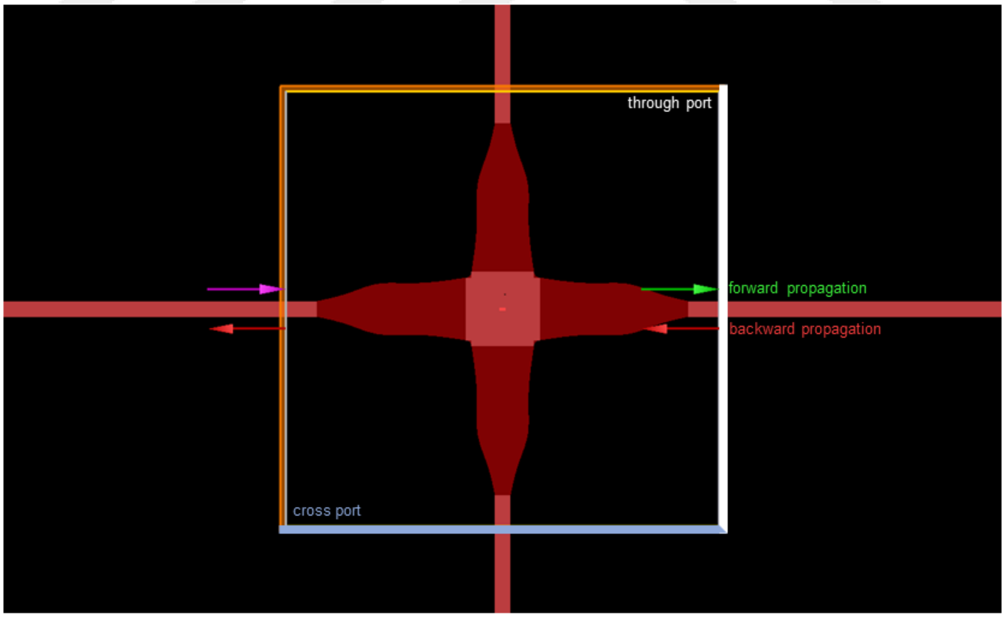

Figure 5.5: The 3D-FDTD simulation layout for the crossing. In the through-port, forward propagating eigenmodes characterize the transmission, and the backward ones determine the reflection. While the crosstalk is calculated in the cross-port.

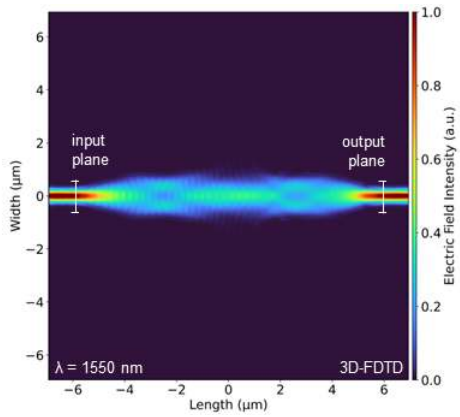

Figure 5.6: 3D-FDTD result where the solid lines indicate the respective input & output planes: a near-lossless match between the input & output fundamental TE modes.

Next, the final geometry's performance is verified with the respective layout in Figure 5.5. Given the fundamental TE-mode input, the resulting electric field intensity demonstrated in Figure 5.6 matches well with the desired mode and doesn't show obvious coupling to the undesired output ports, as determined by the crossing objective.

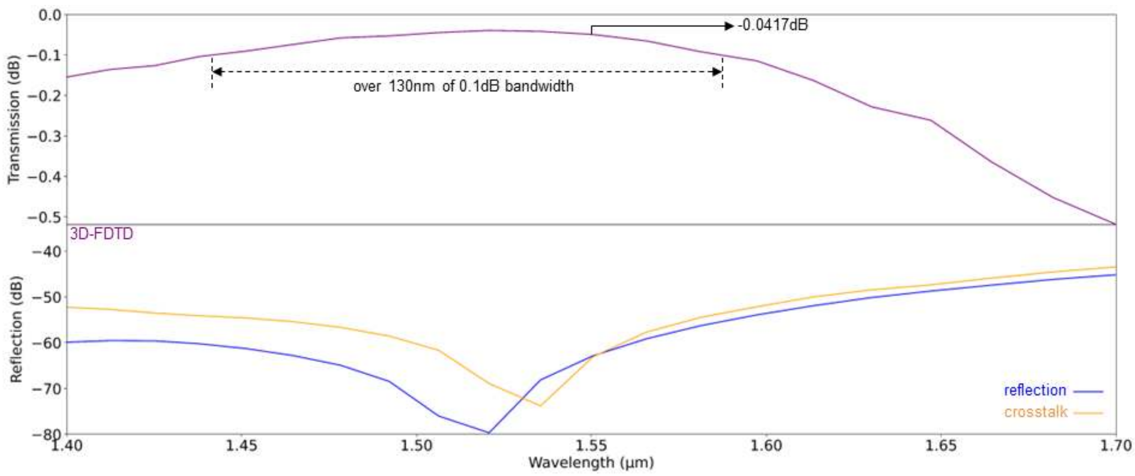

Figure 5.7: Optical spectrum: -0.0417dB transmission at $\lambda = 1550nm$, 0.1dB bandwidth of 130nm with less than 45dB reflection and 43dB crosstalk over the entire band.

As plotted in Figure 5.7, the spectral dependence of the device's transmission indicates a 0.1 dB bandwidth reaching as wide as 130 nm and a 1 dB bandwidth of over 300 nm. Throughout the C-band, it achieves reflection and crosstalk better than -50dB while they remain below -43 dB through 300 nm simulated bandwidth, indicating a broad operation functionality. Although these metrics are calculated for forward propagating modes in the output plane, the objective goal of minimizing coupling to higher-order modes also considers the omnidirectional modes in terms of EME's underlying waveguide physics [Gallagher and Felici, 2003]. Essentially, this explains how the transmission goal can be used as an objective for the reflection and crosstalk.

Crossing performance is evaluated along with the FDTD; tens of crossings are cascaded from their horizontal ports between grating couplers, as illustrated in Figure A.3. Each crossing has the input & output width of 0.5µm, forming the waveguide path. Crossing's spectrum is calculated considering the grating coupler's effect on the input power. Transmission per crossing is evaluated with the best-fit line of the measurements in Figure 5.8. At $\lambda = 1550nm$, the crossing achieves -0.051dB transmission, enabling near-lossless crossing of the input mode. Crossing measurements closely agree with the FDTD over the entire C-band, especially around $\lambda = 1550nm$, as illustrated in Figure 5.9.

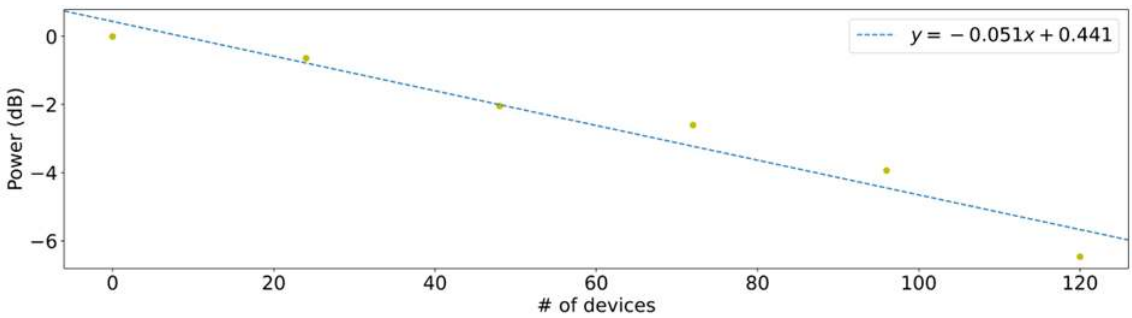

Figure 5.8: Crossing transmission: -51mdB at $\lambda = 1550nm$, in contrast to the -42mdB FDTD result.

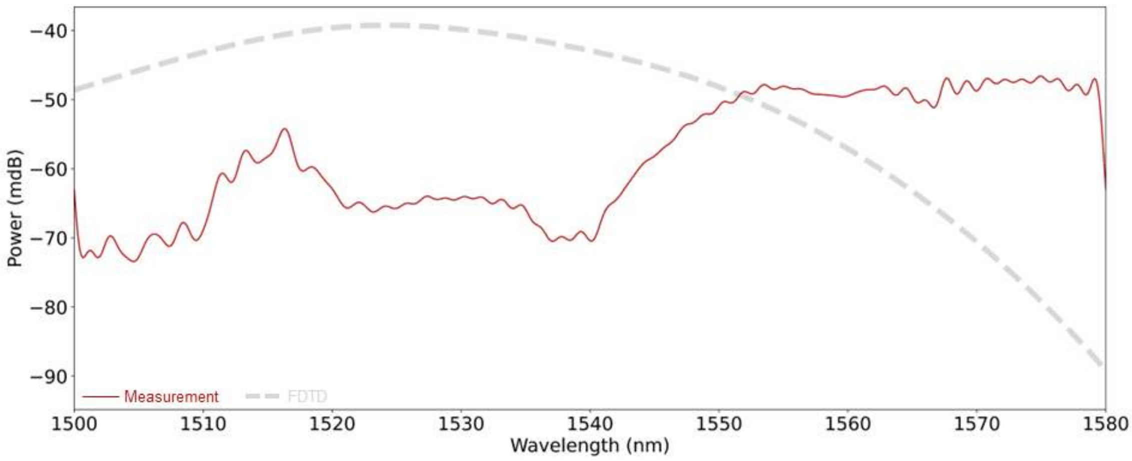

Figure 5.9: Optical spectrum compared with the FDTD spectrum(dashed lines).

Even though some crossings achieve minimal losses below 0.01dB with much narrower bandwidths such as C-band [Dumais et al., 2017, Peng et al., 2021], keeping the low-loss operation on an ultra-wideband stands as an important metric for crossings. The proposed design exhibits comparable transmission performance on much wider simulated bandwidths compared to previously reported SOI waveguide crossings [Michaels et al., 2020, Johnson et al., 2020, Hoffman et al., 2019]. Moreover, ROMEO's proof-of-concept demonstrations remain generalizable to other material platforms and waveguide geometries, where these transmission metrics can be improved using designs with ridge waveguides, materials with smaller refractive index and genetic algorithms [Sanchis et al., 2009, Celo et al., 2014], or subwavelength structures [Wu et al., 2020].

Table 5.1: Comparison of above-mentioned Waveguide Crossings

Work	Footprint (μm^2)	Transmission (mdB)	Thickness (nm)
[Dumais et al., 2017]	30×30 I/O W: 0.5 2×2 center	-7±4 crosstalk: -40dB[C-band]	220
[Peng et al., 2021]	13×13 I/O W: 0.45	-6±2 crosstalk: -55dB[1520-1560nm]	220
[Michaels et al., 2020] λ:1310nm	15×15 I/O W: 0.5 1.7×1.7 center	-75 crosstalk: -38dB[O-band] back reflection: -40dB[O-band]	220\w 110 partial
[Johnson et al., 2020]	14.3×14.3 I/O W: 0.5	-43±4 crosstalk: -50dB[1550-1560nm] backscatter: -55dB[1550-1560nm]	220
[Hoffman et al., 2019]	10×10 I/O W: 0.4	-80 through power -60 dB cross power[1600nm]	250 → 230 during fab.
[Sanchis et al., 2009]	6×6 I/O W: 0.5	-200 crosstalk: -40dB[bw: 20nm] reflection: -40dB[bw: 20nm]	250
[Celo et al., 2014]	6.5×6.5 1.3×1.3 center	-110±20 crosstalk: -45dB[C-band]	220
[Wu et al., 2020] subwavelength grating Both TE & TM	12.5×12.5 I/O W: 0.5 2×2 center	-460(TE) & -640(TM) crosstalk: -35dB both[C-band] back reflection: -13dB both	220
this work	12×12 I/O W: 0.5 2×2 center	-51(fab.)/-42(FDTD) crosstalk: -43dB[1400-1700nm] reflection: -45dB[1400-1700nm]	220

Chapter 6

FUTURE DIRECTIONS AND CONCLUSION

ROMEO also has the potential to extend its applicability to design symmetric waveguides with continuous widths along the propagation axis due to its database structure. This ability also manifests in some devices under development, like the 2×2, 1×3 and 1×4 power splitters. For the 2×2 splitter, it's apparent that the additional S_{mat} introduced for the 1×2 splitter would be sufficient; by adding this S_{mat} in a reverse direction to the beginning of the 1×2 splitter's matrix batch, this device can be realized. Similarly, maximization of the fundamental TE mode could be aimed at the optimization; design would be complete after choosing design parameters; however, this may not be so straightforward for other design candidates. Since the method expresses the performance metrics through the Overall Scatter Matrix it calculates, the objective function is also formed through it. Up to the discussed photonic building blocks, targeting the fundamental TE mode at the output plane would satisfy the desired optical functionality provided with a fundamental TE mode input; yet, these targets are not feasible for all the designs. For example, the power in the output plane should be distributed equally in the split output waveguides to design power splitters. If there are only two output ports, the fundamental TE mode would provide this equal splitting, but for the 1×3 & 1×4 splitters, using only this mode focuses the power on the central output ports as expected. In these cases, the target output field should be a superposition of the output plane's eigenmodes; this requirement brings a multi-mode coupling objective rather than a 100% coupling to the first mode. This objective revision seems to be the main challenge for the future direction of the ROMEO research.

In summary, the proposed EME method significantly improves the computational efficiency of EM simulations. It provides unprecedented accelerations, over five orders of magnitude, in the device simulations, speeding up the whole design procedure to tens of seconds. The reported devices showcase that ROMEO can design adiabatic tapers, 1×2 power splitters, and waveguide crossings. Considering its flexible design parameters and future applicability to potential devices, ROMEO will be a pioneering method that will open new avenues in the design of photonic waveguides.

BIBLIOGRAPHY

[Abdeen et al., 2019] Abdeen, A. S., Attyia, A. M., and Khalil, D. (2019). Compact adiabatic taper for soi waveguide. In *2019 6th International Conference on Advanced Control Circuits and Systems (ACCS) 2019 5th International Conference on New Paradigms in Electronics information Technology (PEIT)*, pages 176–179.

[Asadinia et al., 2021] Asadinia, S., Mehrabi, M., and Yaghoubi, E. (2021). Surix: Non-blocking and low insertion loss micro-ring resonator-based optical router for photonic network on chip. *The Journal of Supercomputing*, 77(5):4438–4460.

[Bogaerts et al., 2020] Bogaerts, W., Pérez, D., Capmany, J., Miller, D. A. B., Poon, J., Englund, D., Morichetti, F., and Melloni, A. (2020). Programmable photonic circuits. *Nature*, 586(7828):207–216.

[Celo et al., 2014] Celo, D., Goodwill, D. J., Dumais, P., Jiang, J., and Bernier, E. (2014). Low-loss waveguide crossings for photonic integrated circuits on soi technology. In *11th International Conference on Group IV Photonics (GFP)*, pages 189–190.

[Chen et al., 2021] Chen, G., Ng, J. D., Lin, H.-L., Zhang, G., Gong, X., and Danner, A. J. (2021). Design and fabrication of high-performance multimode interferometer in lithium niobate thin film. *Opt. Express*, 29(10):15689–15698.

[Christiansen and Sigmund, 2021] Christiansen, R. E. and Sigmund, O. (2021). Inverse design in photonics by topology optimization: tutorial. *J. Opt. Soc. Am. B*, 38(2):496–509.

[Chrostowski, 2024] Chrostowski, L. (2024). Openebl - siepic. `https://siepic.ca/openebl/`.

[Dasdemir et al., 2023] Dasdemir, A. O., Minden, V., and Magden, E. S. (2023). Computational scaling in inverse photonic design through factorization caching. *Applied Physics Letters*, 123(22):221106.

[De la Cruz-Coronado et al., 2020] De la Cruz-Coronado, J. M., Prosopio-Galarza, R., and Rubio-Noriega, R. E. (2020). Silicon photonics foundry-oriented y-junction optimization. In *2020 IEEE XXVII International Conference on Electronics, Electrical Engineering and Computing (INTERCON)*, pages 1–4.

[Dumais et al., 2017] Dumais, P., Goodwill, D. J., Celo, D., Jiang, J., and Bernier, E. (2017). Three-mode synthesis of slab gaussian beam in ultra-low-loss in-plane nanophotonic silicon waveguide crossing. In *2017 IEEE 14th International Conference on Group IV Photonics (GFP)*, pages 97–98.

[Felici and Engl, 2001] Felici, T. and Engl, H. W. (2001). On shape optimization of optical waveguides using inverse problem techniques. *Inverse Problems*, 17(4):1141.

[Feng et al., 2024] Feng, H., Ge, T., Guo, X., Wang, B., Zhang, Y., Chen, Z., Zhu, S., Zhang, K., Sun, W., Huang, C., Yuan, Y., and Wang, C. (2024). Integrated lithium niobate microwave photonic processing engine. *Nature*, 627(8002):80–87.

[Gallagher and Felici, 2003] Gallagher, D. F. G. and Felici, T. P. (2003). Eigenmode expansion methods for simulation of optical propagation in photonics: pros and cons. In Sidorin, Y. S. and Tervonen, A., editors, *Integrated Optics: Devices, Materials, and Technologies VII*, volume 4987, pages 69 – 82. International Society for Optics and Photonics, SPIE.

[Garza and Sideris, 2023] Garza, E. and Sideris, C. (2023). Fast inverse design of 3d nanophotonic devices using boundary integral methods. *ACS Photonics*, 10(4):824–835.

[Goel et al., 2024] Goel, S., Leedumrongwatthanakun, S., Valencia, N. H., McCutcheon, W., Tavakoli, A., Conti, C., Pinkse, P. W. H., and Malik, M. (2024).

Inverse design of high-dimensional quantum optical circuits in a complex medium. *Nature Physics*, 20(2):232–239.

[Hammond et al., 2022] Hammond, A. M., Oskooi, A., Chen, M., Lin, Z., Johnson, S. G., and Ralph, S. E. (2022). High-performance hybrid time/frequency-domain topology optimization for large-scale photonics inverse design. *Opt. Express*, 30(3):4467–4491.

[Hoffman et al., 2019] Hoffman, G. B., Dallo, C., Starbuck, A., Hood, D., Pomerene, A., Trotter, D., and DeRose, C. T. (2019). Improved broadband performance of an adjoint shape optimized waveguide crossing using a levenberg-marquardt update. *Opt. Express*, 27(17):24765–24780.

[Johnson et al., 2020] Johnson, M., Thompson, M. G., and Sahin, D. (2020). Low-loss, low-crosstalk waveguide crossing for scalable integrated silicon photonics applications. *Opt. Express*, 28(9):12498–12507.

[Lalau-Keraly et al., 2013] Lalau-Keraly, C. M., Bhargava, S., Miller, O. D., and Yablonovitch, E. (2013). Adjoint shape optimization applied to electromagnetic design. *Opt. Express*, 21(18):21693–21701.

[Lin and Shi, 2019] Lin, Z. and Shi, W. (2019). Broadband, low-loss silicon photonic y-junction with an arbitrary power splitting ratio. *Opt. Express*, 27(10):14338–14343.

[Liu et al., 2022] Liu, Y., Qiu, Z., Ji, X., Lukashchuk, A., He, J., Riemensberger, J., Hafermann, M., Wang, R. N., Liu, J., Ronning, C., and Kippenberg, T. J. (2022). A photonic integrated circuit–based erbium-doped amplifier. *Science*, 376(6599):1309–1313.

[Lumerical, 2024] Lumerical (2024). Lumerical. `https://www.lumerical.com/`.

[Magden, 2024] Magden, E. S. (2024). Photonic architecture laboratories. `https://pal.ku.edu.tr/`.

[Mao et al., 2023] Mao, S., Cheng, L., Chen, H., Liu, X., Geng, Z., Li, Q., and Fu, H. (2023). Multi-task topology optimization of photonic devices in low-dimensional fourier domain via deep learning. *Nanophotonics*, 12(5):1007–1018.

[Michaels et al., 2020] Michaels, A., Wu, M. C., and Yablonovitch, E. (2020). Hierarchical design and optimization of silicon photonics. *IEEE Journal of Selected Topics in Quantum Electronics*, 26(2):1–12.

[Michaels and Yablonovitch, 2018] Michaels, A. and Yablonovitch, E. (2018). Leveraging continuous material averaging for inverse electromagnetic design. *Opt. Express*, 26(24):31717–31737.

[Mishkin and Matas, 2016] Mishkin, D. and Matas, J. (2016). All you need is a good init. In *International Conference on Learning Representations 2016*.

[Nguyen et al., 2019] Nguyen, H. V., Kim, I. K., and Seok, T. J. (2019). Low-loss and broadband silicon photonic y- junction using tapered rib waveguides. In *2019 International Conference on Optical MEMS and Nanophotonics (OMN)*, pages 76–77.

[NLopt, 2024] NLopt (2024). Nlopt documentation. `https://nlopt.readthedocs.io/en/latest/`.

[Oktay et al., 2022] Oktay, M. C., Aydogan, A., and Magden, E. S. (2022). Efficient waveguide taper design with rapid and data-driven eigenmode expansion. In *2022 Photonics North (PN)*, pages 1–1.

[Oktay et al., 2024a] Oktay, M. C., Aydogan, A., and Magden, E. S. (2024a). Machine-learning-based integrated photonic device optimization with data-driven eigenmode expansion. In García-Blanco, S. M. and Cheben, P., editors, *Integrated Optics: Devices, Materials, and Technologies XXVIII*, volume 12889, page 128890M. International Society for Optics and Photonics, SPIE.

[Oktay et al., 2024b] Oktay, M. C., Gorgulu, K., and Magden, E. S. (2024b). Computationally efficient nanophotonic design through data-driven eigenmode expansion. *Journal of Lightwave Technology*, pages 1–9.

[Peng et al., 2021] Peng, Y., Li, H., and Dai, D. (2021). Compact silicon photonic waveguide crossings with sub-10-mdb loss. In *2021 Asia Communications and Photonics Conference (ACP)*, pages 1–3.

[Photonics, 2024] Photonics, M. L. (2024). Maple leaf photonics. `https://www.mapleleafphotonics.com/`.

[Powell, 2007] Powell, M. J. D. (2007). A view of algorithms for optimization without derivatives. *Mathematics TODAY*, 43.

[Redheffer, 1961] Redheffer, R. (1961). *Difference equations and functional equations in transmission-line theory*, volume 12. McGraw-Hill, New York, NY, modern mathematics for the engineer, e. f. beckenbach edition.

[Riveros et al., 2021] Riveros, L. G. M., Lucia, F. L. D., Bustamante, Y. R. R., de Andrade, H. A., Sutili, T., and Figueiredo, R. C. (2021). Optical grating coupling on silicon photonics based on metallized angle-polished fibers. In *2021 SBFoton International Optics and Photonics Conference (SBFoton IOPC)*, pages 1–4.

[Sanchis et al., 2009] Sanchis, P., Villalba, P., Cuesta, F., Håkansson, A., Griol, A., Galán, J. V., Brimont, A., and Martí, J. (2009). Highly efficient crossing structure for silicon-on-insulator waveguides. *Opt. Lett.*, 34(18):2760–2762.

[SciPy, 2024] SciPy (2024). scipy.interpolate.cubicspline. `https://docs.scipy.org/doc/scipy/reference/generated/scipy.interpolate.CubicSpline.html`.

[Sethi et al., 2017] Sethi, P., Haldar, A., and Selvaraja, S. K. (2017). Ultra-compact low-loss broadband waveguide taper in silicon-on-insulator. *Opt. Express*, 25(9):10196–10203.

[Shekhar et al., 2024] Shekhar, S., Bogaerts, W., Chrostowski, L., Bowers, J. E., Hochberg, M., Soref, R., and Shastri, B. J. (2024). Roadmapping the next generation of silicon photonics. *Nature Communications*, 15(1):751.

[Stewart, 1998] Stewart, G. W. (1998). *Matrix Algorithms Volume I Basic Decompositions.*

[Sutskever et al., 2013] Sutskever, I., Martens, J., Dahl, G., and Hinton, G. (2013). On the importance of initialization and momentum in deep learning. In Dasgupta, S. and McAllester, D., editors, *Proceedings of the 30th International Conference on Machine Learning*, volume 28 of *Proceedings of Machine Learning Research*, pages 1139–1147, Atlanta, Georgia, USA. PMLR.

[Tang et al., 2023] Tang, R. J., Lim, S. W. D., Ossiander, M., Yin, X., and Capasso, F. (2023). Time reversal differentiation of fdtd for photonic inverse design. *ACS Photonics*, 10(12):4140–4150.

[Wu et al., 2020] Wu, S., Mao, S., Zhou, L., Liu, L., Chen, Y., Mu, X., Cheng, L., Chen, Z., Tu, X., and Fu, H. Y. (2020). A compact and polarization-insensitive silicon waveguide crossing based on subwavelength grating mmi couplers. *Opt. Express*, 28(19):27268–27276.

[Wu et al., 2023] Wu, T., Menarini, M., Gao, Z., and Feng, L. (2023). Lithography-free reconfigurable integrated photonic processor. *Nature Photonics*, 17(8):710–716.

[Yeung et al., 2023] Yeung, C., Pham, B., Tsai, R., Fountaine, K. T., and Raman, A. P. (2023). Deepadjoint: An all-in-one photonic inverse design framework integrating data-driven machine learning with optimization algorithms. *ACS Photonics*, 10(4):884–891.

[Zhang et al., 2013] Zhang, Y., Yang, S., Lim, A. E.-J., Lo, G.-Q., Galland, C., Baehr-Jones, T., and Hochberg, M. (2013). A compact and low loss y-junction for submicron silicon waveguide. *Opt. Express*, 21(1):1310–1316.

Appendix A

METHODS

The below-mentioned methods are conducted in an openEbL [Chrostowski, 2024].

A.1 Fabrication

All the waveguides are designed in KLayout with the SiEPIC EBeam PDK package on a single mask. For the waveguide taper, devices are mirrored and cascaded between the grating couplers, as shown in Figure A.1. Adding strips to extend the split output waveguides, 1×2 power splitters are again mirrored and cascaded, as illustrated in Figure A.2. Lastly, waveguide crossings are cascaded by their horizontal ports, as displayed in Figure A.3. 100keV JEOL 8100FS Electron Beam Lithography fabricates the single-etch 220nm-thick SOI wafer.

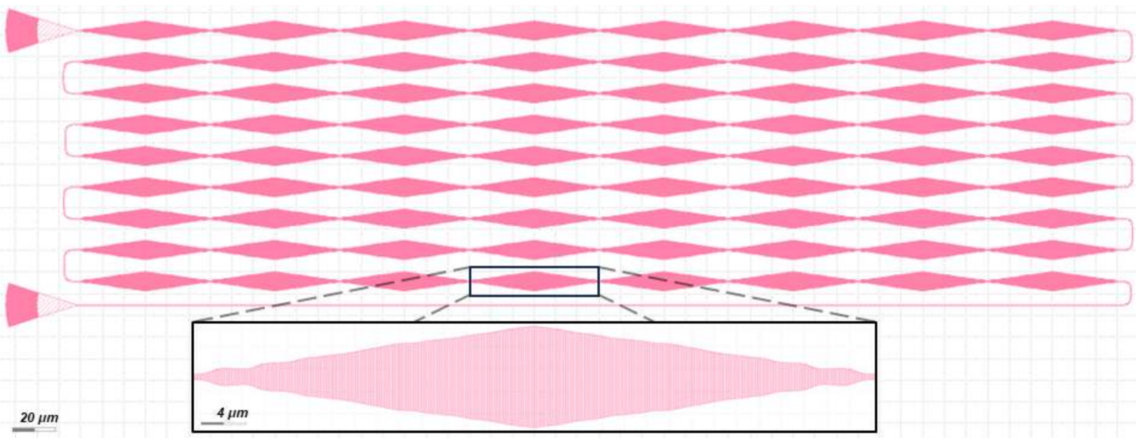

Figure A.1: Taper Mask Layout: Devices are paired from their output planes and cascaded.

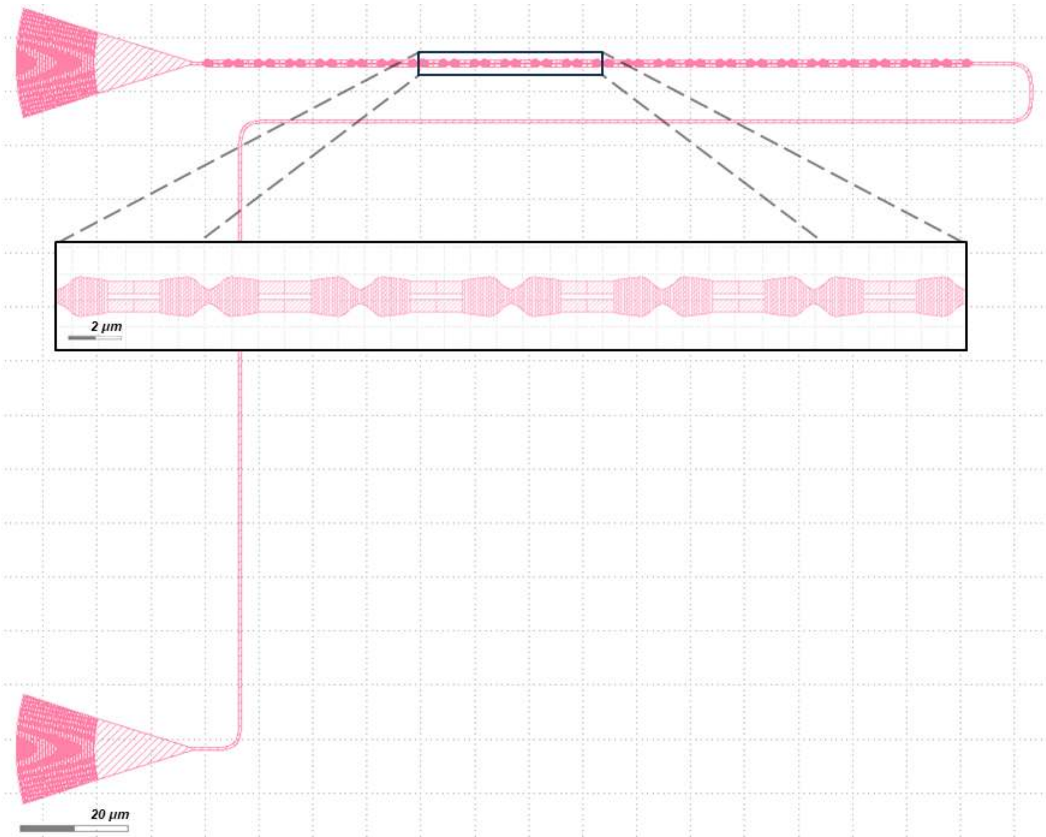

Figure A.2: Splitter Mask Layout: Devices are grouped with split output waveguides and cascaded.

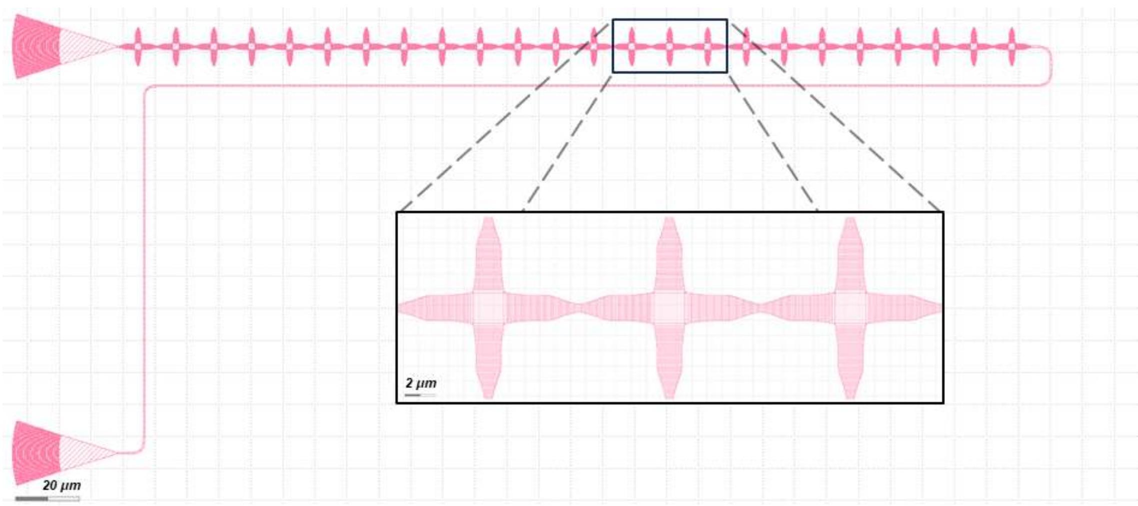

Figure A.3: Crossing Mask Layout: Devices are cascaded from their horizontal ports.

A.2 Testing & Measurements

Testing of the fabricated mask is conducted with Maple Leaf Photonics probe stations [Photonics, 2024]. The structure of the respective PDK allows an upper layer of labels to automate the measurements, as exemplified in Figure A.4.

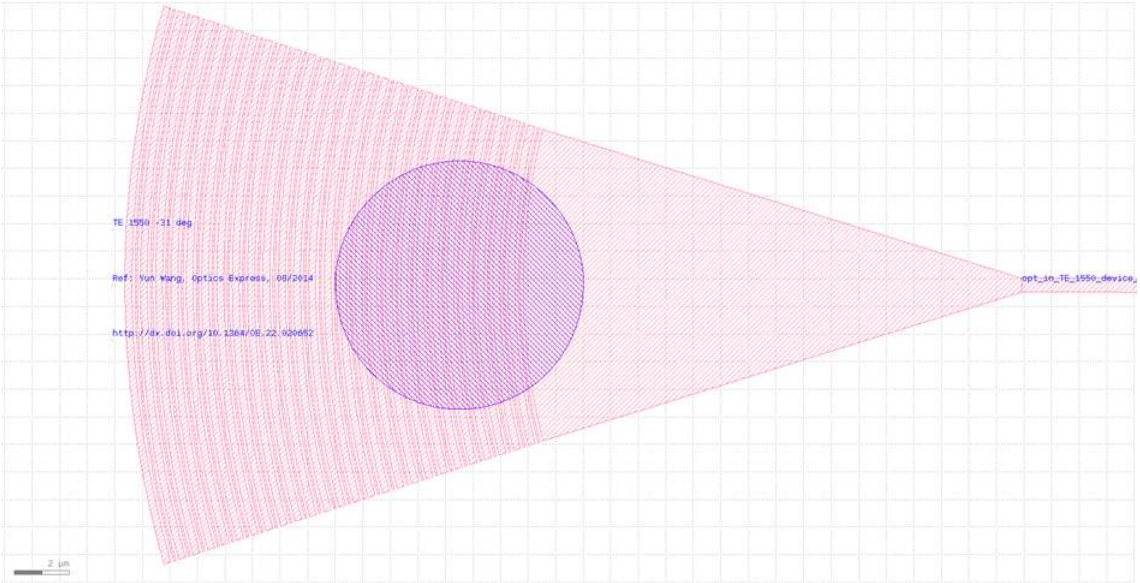

Figure A.4: Labels prepare the grating coupler for probing.

During the measurements, grating couplers are used as input & output channels, as demonstrated in Figure A.5. The probe station aligns itself to provide the fundamental TE mode within the C-band ($1500nm < \lambda < 1580nm$) at 25°C to the 0.5μm x 0.22μm cross-sectional waveguide strip, as a similar setup is photographed in Figure A.6. HP81680A modules are used for the laser, which has 3dBm power and 40nm/s sweeping speed, and the HP81635A modules detect the signals.

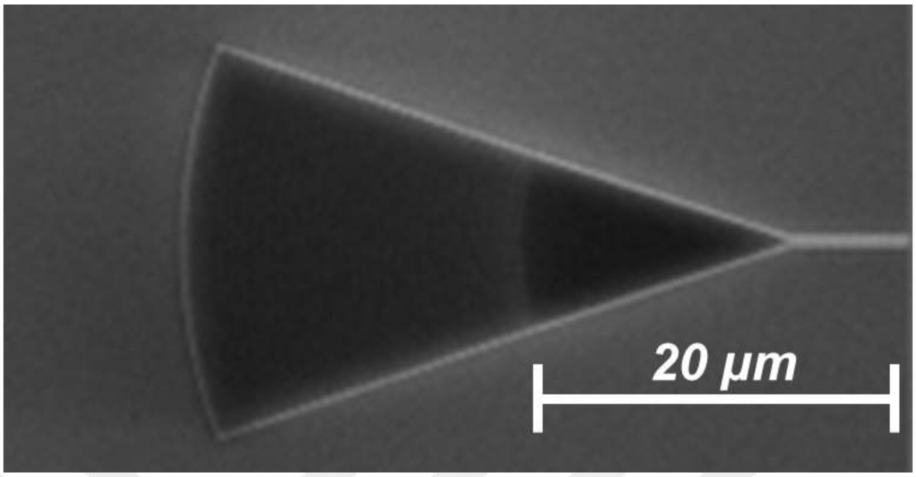

Figure A.5: Fabricated Grating Coupler: SEM image.

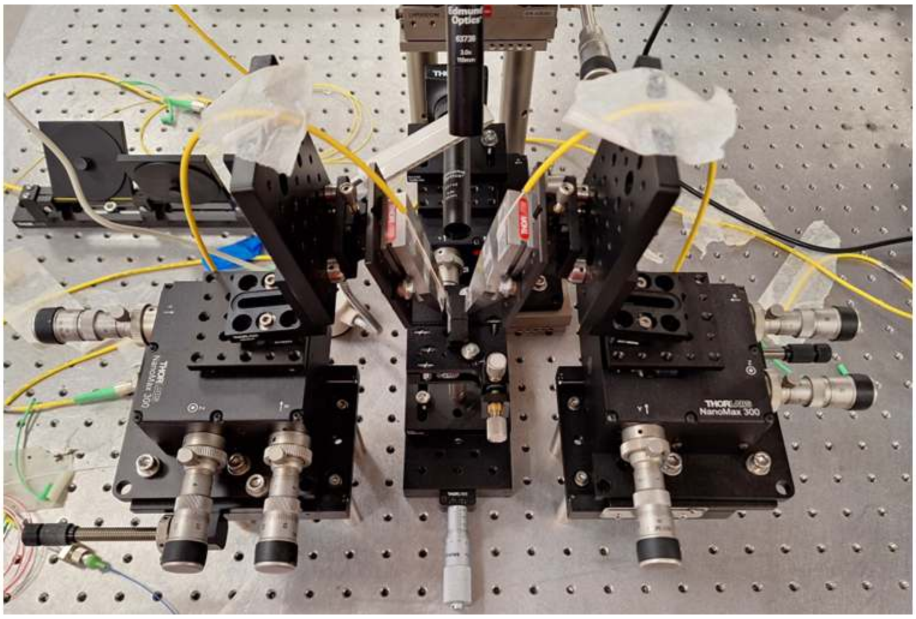

Figure A.6: Representative testing setup from Photonic Architecture Laboratories [Magden, 2024].